

Experimental evidence of stable wave patterns on deep water*

DIANE M. HENDERSON¹†, HARVEY SEGUR²,
AND JOHN D. CARTER³

¹Department of Mathematics, Penn State University, University Park, PA 16803, USA

²Department of Applied Mathematics, University of Colorado, Boulder, CO 80309, USA

³Mathematics Department, Seattle University, Seattle, WA 98122, USA

(Received 1 June 2009; revised 2 April 2010; accepted 2 April 2010)

Recent predictions from competing theoretical models have disagreed about the stability/instability of bi-periodic patterns of surface waves on deep water. We present laboratory experiments to address this controversy. Growth rates of modulational perturbations are compared to predictions from: (i) inviscid coupled nonlinear Schrödinger (NLS) equations, according to which the patterns are unstable and (ii) dissipative coupled NLS equations, according to which they are linearly stable. For bi-periodic wave patterns of small amplitude and nearly permanent form, we find that the dissipative model predicts the experimental observations more accurately. Hence, our experiments support the claim that these bi-periodic wave patterns are linearly stable in the presence of damping. For bi-periodic wave patterns of large enough amplitude or subject to large enough perturbations, both models fail to predict accurately the observed behaviour, which includes frequency downshifting.

Key words: stability, surface gravity waves

1. Introduction and main conclusions

Surface waves on deep water have been described in terms of plane waves of permanent form, with one-dimensional surface patterns, at least since Stokes (1847, 1966). Less is known about deep-water waves with two-dimensional surface patterns (so the velocity fields are three-dimensional), like those shown in figure 1. Approximate models of wave patterns like these date back to the 1950s (Fuchs 1952; Chappelear 1959), but mathematical proof of the existence of such wave patterns is much more recent (Craig & Nicholls 2000, 2002; Iooss & Plotnikov 2009). Detailed experimental studies of wave patterns like these are also more recent (Kimmoun, Branger & Kharif 1999; Hammack, Henderson & Segur 2005; Henderson, Patterson & Segur 2006).

An important aspect of the studies of two-dimensional wave patterns of permanent form on deep water has been their stability. Roskes (1976), using coupled nonlinear Schrödinger (NLS) equations, and Dhar & Das (1991), using coupled Dysthe-type equations (Dysthe 1979), both without dissipation and allowing only one-dimensional perturbations, showed that two-dimensional wave patterns of permanent form on deep water are unstable because of a modulational instability. (The modulational

*With an appendix by Abhijit Chaudhuri and Erin Byrne

† Email address for correspondence: dmh@math.psu.edu

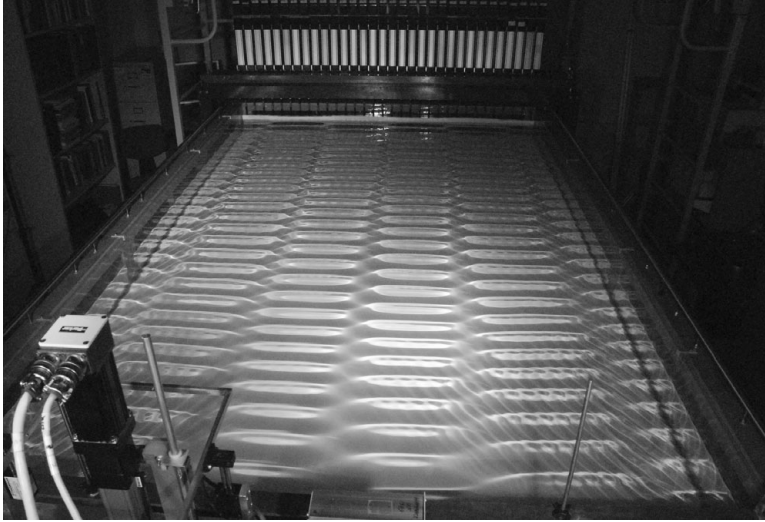


FIGURE 1. Photograph of bi-periodic surface waves with frequency 4 Hz and wavelength in the direction of propagation of about 10 cm.

instability had been discovered earlier for plane waves by Benjamin & Feir 1967, Ostrovsky 1967 and Zakharov 1968.) Roskes (1976) and Dhar & Das (1991) showed that the modulational instability is not restricted to plane waves. Their predictions of instability were later generalized to allow two-dimensional perturbations, again without dissipation, by Ioualalen & Kharif (1994), Baludin *et al.* (1995) and Leblanc (2009). Baludin *et al.* (1995) made a point of relating their analysis to earlier work on stability, in several contexts. More recently, some of these results were re-derived by Onorato, Osborne & Serio (2006) and Shukla *et al.* (2006), using coupled (i.e. vector) nonlinear Schrödinger (VNLS) models, without dissipation. These instabilities are also studied in a numerical investigation of two-dimensional surface patterns in deep water using a Boussinesq-type model by Fuhrman, Madsen & Bingham (2006). Craig *et al.* (2007) also predicted this: waves with two-dimensional surface patterns are unstable in a VNLS model without dissipation. But they also predicted that any amount of dissipation stabilizes the instability. This lack of agreement among theoretical models on the stability/instability of waves with two-dimensional surface patterns on deep water motivated the experimental study described herein.

Experimental evidence of the stability/instability of bi-periodic wave patterns was discussed qualitatively by Kimmoun *et al.* (1999), Hammack *et al.* (2005) and Henderson *et al.* (2006), with related information by Fuhrman & Madsen (2006). To our knowledge, the results presented herein provide the first experimental, quantitative test of predictions of stability/instability of bi-periodic wave patterns on deep water. We present laboratory experiments that test the predictions of stability/instability according to two models: (i) a non-dissipative VNLS model with a dissipative correction added *a posteriori* and (ii) a dissipative VNLS model, which allows the dissipation to interact with the other terms in the model. The first model predicts effective instability whenever the growth rate of the (non-dissipative) instability exceeds the decay rate due to dissipation. The prediction of the second model is less intuitive: it predicts linear stability for any positive dissipation rate, including

very small rates. (For very small dissipation rates, long distances are required to observe the total growth of the perturbation, so a long test section is required to determine stability/instability experimentally.)

All of our experiments were conducted in the wave tank shown in figure 1. A limitation of this facility is that the tank is relatively short (12 ft from the wavemakers to the other end of the tank). As a result, our experiments were able to discriminate between the predictions of the competing models only if the dissipation rate was relatively high, so that the relevant dynamics occurred over a relatively short distance. Therefore, we are unable to test in our facility the most intriguing point of disagreement of the competing theoretical models: whether dissipation can stabilize the modulational instability, even for very small dissipation rates.

Here is what we can do. For a fixed dissipation rate, each model predicts not only stability versus instability, but also the detailed evolution of the entire wave system. Thus, for that dissipation rate, we compare the observed evolution in the wave tank with the evolution predicted by each theory. We determine which model more accurately predicts the evolution observed in the tank, at that dissipation rate. This way, we can decide which of the two competing models is more accurate, at each dissipation rate for which our experiments are conclusive.

We show below that for wave patterns with small to moderate amplitudes and subject to small enough perturbations, the dissipative VNLS model predicts the experimental data more accurately than does the non-dissipative model, even after a dissipative correction. Thus, our experiments favour the dissipative model as more accurate; so they also favour its conclusion: bi-periodic wave patterns are linearly stable in the presence of dissipation, at least when dissipation is large enough. The dissipative VNLS model predicts linear stability for any positive dissipation rate; our experiments corroborate this prediction for strong dissipation and are inconclusive for weak dissipation.

We also show that without linearizing the two models in question, the dissipative VNLS model predicts the measured wave evolution more accurately than does the non-dissipative model, even after adding a dissipative correction to that model. The inaccuracy of the non-dissipative VNLS model is most striking in its predictions of the evolution of the carrier wave itself: the non-dissipative VNLS model predicts large oscillations of the carrier-wave amplitude, which do not occur in the measured data.

Finally, we show that for wave patterns with large enough amplitude or for patterns subjected to large enough perturbations, neither of these VNLS models, with or without dissipation, describes the experimental results accurately: the measured wave patterns show frequency downshifting (e.g. Lake *et al.* 1977), not predicted by either model. Neither the non-dissipative nor the dissipative VNLS model applies to the large-amplitude experiments because both models conserve an integral of the motion that the large-amplitude experiments do not conserve. The observation that spatially periodic wave patterns of large amplitude experience frequency downshifting that is not included in the models demotes any issue about the stability/instability of bi-periodic wave patterns of large amplitude to a non-central issue. Our results for two-dimensional wave patterns, like that in figure 1, are consistent with the earlier results of Segur *et al.* (2005):

- (i) for wave patterns of small to moderate amplitude, dissipation is required in NLS-type models for agreement with experiments;
- (ii) for wave patterns of large amplitude, NLS-type models, with or without dissipation, simply do not apply.

We expect these stability results to apply to any physical system that uses NLS-type equations to model the evolution of waves of small to moderate amplitude, subject to small perturbations: even small damping can stabilize the modulational instability. For large-amplitude waves or perturbations, one should consider the possibility that downshifting and a breakdown of the applicability of the NLS-type model might occur, as it does in water waves. Other such systems include nonlinear optics (Ostrovsky 1967; Zakharov 1967; Anderson & Lisak 1984; Tai, Tomita & Hasegawa 1986; Hasegawa & Kodama 1995), and plasmas (Hasegawa 1972; McKinstrie & Bingham 1989).

In the following, we review the results from the dissipative and non-dissipative VNLS models for two interacting wavetrains as well as how to apply these models to experimental data in §2, describe the experimental procedures in §3 and present the comparison of predictions and experimental measurements in §4. We briefly sum up the results and make concluding remarks in §5.

2. Theoretical considerations

We wish to study the stability of wave patterns like that shown in figure 1. To do so, we consider the stability of uniform wavetrain solutions to two VNLS models: one with and one without dissipation. In this section, we present the theoretical results from these two models (§2.1) and show how we use these results to make predictions for quantitative comparison with symmetric experiments (§2.2).

2.1. Results from VNLS models

The wave pattern in figure 1 was generated using two wavetrains with the same frequency and amplitude propagating at an oblique angle to each other, resulting in a symmetric bi-periodic surface pattern. More generally, we may allow for two carrier waves with arbitrary parameters, so that the water-surface displacement, $\eta(x, y, t)$, may be described at leading order (in a formal σ -expansion) as their sum:

$$\eta(x, y, t; \sigma) = 2\sigma [|\hat{A}| \sin(k_A x + l_A y - \omega_A t + \hat{\phi}_A) + |\hat{B}| \sin(k_B x + l_B y - \omega_B t + \hat{\phi}_B)] + O(\sigma^2), \quad (2.1)$$

where $\sigma \ll 1$ is a measure of weak nonlinearity, $k_{A/B}$ and $l_{A/B}$ are the x and y wavenumbers of the A th and B th carrier waves, $\omega_{A/B}$ are their frequencies and the complex envelope amplitudes $i\hat{A}(X, Y, T) = |\hat{A}|e^{i\hat{\phi}_A}$ and $i\hat{B}(X, Y, T) = |\hat{B}|e^{i\hat{\phi}_B}$ vary on slow scales $X = \sigma x$, $Y = \sigma y$ and $T = \sigma t$. Under the assumptions that we have two wavetrains on deep water that are weakly nonlinear, nearly monochromatic and subject to weak exponential-type damping, the standard method of multiple scales (see, for example, Hammack *et al.* 2005) results in coupled evolution equations for the (complex) amplitudes:

$$i(\partial_T \hat{A} + c_A \partial_X \hat{A} + d_A \partial_Y \hat{A}) + \sigma [\alpha_A \partial_{XX} \hat{A} + \beta_A \partial_{YY} \hat{A} + \gamma_A \partial_{XY} \hat{A} + \xi_A |\hat{A}|^2 \hat{A} + \zeta_{AB} |\hat{B}|^2 \hat{A}] + i\sigma \delta_A \hat{A} = 0, \quad (2.2a)$$

$$i(\partial_T \hat{B} + c_B \partial_X \hat{B} + d_B \partial_Y \hat{B}) + \sigma [\alpha_B \partial_{XX} \hat{B} + \beta_B \partial_{YY} \hat{B} + \gamma_B \partial_{XY} \hat{B} + \xi_B |\hat{B}|^2 \hat{B} + \zeta_{BA} |\hat{A}|^2 \hat{B}] + i\sigma \delta_B \hat{B} = 0. \quad (2.2b)$$

Here $c_{A/B}$ and $d_{A/B}$ are the x and y components of the group velocities of the A th and B th waves, $\alpha_{A/B}$, $\beta_{A/B}$ and $\gamma_{A/B}$ are constants depending on the dispersion relation between the carrier-wave frequencies and wavenumbers, $\xi_{A/B}$ are self-coupling coefficients, $\zeta_{AB/BA}$ are cross-coupling coefficients between the two carrier waves and dissipation is included through the linear damping rates, δ_A and δ_B . The dissipative terms in (2.2), which lead to exponential damping, can be derived from the Navier–Stokes equations (cf. Miles 1967; Dias, Dyachenko & Zakharov 2008). We use this form of damping in this study because it agrees with observations. (See, for example, figure 4a of this paper or Appendix A of Segur *et al.* 2005.) It has been used in the scalar version of (2.2), for which $\hat{B} \equiv 0$, by Lake *et al.* (1977) and Mei & Hancock (2003) for water waves and in optics by Luther & McKinstrie (1990), Hasegawa & Kodama (1995) and Karlsson (1995).

With no dissipation, $\delta_A = \delta_B \equiv 0$, so that (2.2) become the (non-dissipative) VNLS equations, used, for example, by Benney & Newell (1967), Hammack *et al.* (2005), Onorato *et al.* (2006), Shukla *et al.* (2006) and Craig *et al.* (2007).

A referee brought to our attention that (2.2) are derived in the limit $\sigma \rightarrow 0$, but they still contain σ . As we show in §2.2, the factor σ in (2.2) scales out when we restrict our attention to symmetric wave patterns with symmetric perturbations. Pierce & Knobloch (1994) overcame the problem of a σ -dependent model for counter-propagating wavetrains differently, at the cost of introducing non-local terms into the equations. Their idea was generalized by Bridges & Laine-Pearson (2005), who studied the stability of short-crested waves, like those considered here, and obtained similar results without using non-local terms. Both of these papers assume no dissipation.

Craig *et al.* (2007) also considered the dissipative case ($\delta_A > 0, \delta_B > 0$), for which it is convenient to recast the system to one that factors out the exponential decay. Following their analysis, we make the change of variables:

$$\left. \begin{aligned} \hat{A}(X, Y, T; \sigma) &= e^{-\sigma\delta_A T} A, \\ \hat{B}(X, Y, T; \sigma) &= e^{-\sigma\delta_B T} B. \end{aligned} \right\} \quad (2.3)$$

Then (2.2) becomes

$$\begin{aligned} i(\partial_T A + c_A \partial_X A + d_A \partial_Y A) + \sigma [\alpha_A \partial_{XX} A + \beta_A \partial_{YY} A + \gamma_A \partial_{XY} A \\ + \xi_A e^{-2\sigma\delta_A T} |A|^2 A + \zeta_{AB} e^{-2\sigma\delta_B T} |B|^2 A] = 0, \end{aligned} \quad (2.4a)$$

$$\begin{aligned} i(\partial_T B + c_B \partial_X B + d_B \partial_Y B) + \sigma [\alpha_B \partial_{XX} B + \beta_B \partial_{YY} B + \gamma_B \partial_{XY} B \\ + \xi_B e^{-2\sigma\delta_B T} |B|^2 B + \zeta_{BA} e^{-2\sigma\delta_A T} |A|^2 B] = 0. \end{aligned} \quad (2.4b)$$

All of the coefficients in (2.4), except for the damping rates (discussed below), are the same as in (2.2). These coefficients have been derived by Dhar & Das (1991) and others, for pure gravity waves. Here we include the effects of both gravity and surface tension, as listed in Appendix A.

In our laboratory experiments (§§3 and 4), we measure time series at fixed x -locations at increasing distances from the wavemaker, so that evolution is measured with respect to x . For comparison with data, we re-cast the above equations by interchanging the roles of (X, T) , making X the evolution variable. To do this, we use

the ordering prescribed by (2.4) which gives

$$\left. \begin{aligned} \frac{\partial A}{\partial X} &= -\frac{1}{c_A} \left(\frac{\partial A}{\partial T} + d_A \frac{\partial A}{\partial Y} \right) + O(\sigma), \\ \frac{\partial B}{\partial X} &= -\frac{1}{c_B} \left(\frac{\partial B}{\partial T} + d_B \frac{\partial B}{\partial Y} \right) + O(\sigma), \end{aligned} \right\} \quad (2.5)$$

so that to VNLS order, (2.3) becomes

$$\left. \begin{aligned} \hat{A}(X, Y, T; \sigma) &= e^{-\sigma \tilde{\delta}_A X} A, \\ \hat{B}(X, Y, T; \sigma) &= e^{-\sigma \tilde{\delta}_B X} B, \end{aligned} \right\} \quad (2.6)$$

where $\tilde{\delta}_A = \delta_A/c_A$ and $\tilde{\delta}_B = \delta_B/c_B$. The δ -VNLS equations (2.4) become

$$\begin{aligned} i(\partial_T A + c_A \partial_X A + d_A \partial_Y A) + \sigma [\tilde{\alpha}_A \partial_{TT} A + \tilde{\beta}_A \partial_{YY} A + \tilde{\gamma}_A \partial_{TY} A \\ + \xi_A e^{-2\sigma \tilde{\delta}_A X} |A|^2 A + \zeta_{AB} e^{-2\sigma \tilde{\delta}_B X} |B|^2 A] = 0, \end{aligned} \quad (2.7a)$$

$$\begin{aligned} i(\partial_T B + c_B \partial_X B + d_B \partial_Y B) + \sigma [\tilde{\alpha}_B \partial_{TT} B + \tilde{\beta}_B \partial_{YY} B + \tilde{\gamma}_B \partial_{TY} B \\ + \xi_B e^{-2\sigma \tilde{\delta}_B X} |B|^2 B + \zeta_{BA} e^{-2\sigma \tilde{\delta}_A X} |A|^2 B] = 0, \end{aligned} \quad (2.7b)$$

where $\tilde{\alpha}_A = \alpha_A/c_A^2$, $\tilde{\beta}_A = \beta_A - \gamma_A d_A/c_A + \alpha_A d_A^2/c_A^2$ and $\tilde{\gamma}_A = -\gamma_A/c_A + 2\alpha_A d_A/c_A^2$, with analogous new B -coefficients. We refer to the dissipative models, (2.4) and (2.7), as the δ -VNLS equations.

As with VNLS (i.e. (2.2) with $\delta_A = \delta_B = 0$), the δ -VNLS systems in (2.4) and (2.7) are Hamiltonian, but the Hamiltonians of (2.4) and (2.7) are not conserved. Important features of Hamiltonian systems are their conserved quantities, two of which we use in these experiments. In terms of X -evolution, the dissipative system (2.7), as well as its non-dissipative counterpart, conserve

$$M = \int \int (|A|^2 + |B|^2) dT dY, \quad (2.8a)$$

$$\mathbf{P} = \frac{1}{b} \int \int [(A \nabla A^* - A^* \nabla A) + (B \nabla B^* - B^* \nabla B)] dT dY, \quad (2.8b)$$

where $\nabla = (\partial_T, \partial_Y)$ and, for the symmetric experiments considered in §§ 2.2, 3 and 4, $b = \omega_p$ is the difference between the carrier-wave frequency, ω , and the seeded perturbation frequencies, $\omega \pm \omega_p$. We use this factor of b in our definition of \mathbf{P} so that M and \mathbf{P} have the same units, and measurements can be graphed on the same scale.

As we discuss in § 3, we are able to measure accurately only one component of \mathbf{P} in (2.8b), which is

$$P_x = \frac{1}{b} \int \int [(A \partial_T A^* - A^* \partial_T A) + (B \partial_T B^* - B^* \partial_T B)] dT dY. \quad (2.9)$$

A solution of (2.7) corresponding to a bi-periodic pattern of waves with amplitudes uniform in Y and T is $A(X) = |A_0|\psi_A(X)$ and $B(X) = |B_0|\psi_B(X)$, where

$$\left. \begin{aligned} \psi_A(X) &= \exp \left[i \frac{\xi_A}{2\tilde{\delta}_{AC_A}} |A_0|^2 (1 - e^{-2\sigma\tilde{\delta}_A X}) + i \frac{\zeta_{AB}}{2\tilde{\delta}_{BC_A}} |B_0|^2 (1 - e^{-2\sigma\tilde{\delta}_B X}) + i(\phi_1 + \phi_2) \right], \\ \psi_B(X) &= \exp \left[i \frac{\xi_B}{2\tilde{\delta}_{BC_B}} |B_0|^2 (1 - e^{-2\sigma\tilde{\delta}_B X}) + i \frac{\zeta_{BA}}{2\tilde{\delta}_{AC_B}} |A_0|^2 (1 - e^{-2\sigma\tilde{\delta}_A X}) + i(\phi_1 - \phi_2) \right], \end{aligned} \right\} \quad (2.10)$$

and $\phi_1 \pm \phi_2$ are convenient forms for the initial phases of the A/B waves. We show below that the unperturbed wave pattern shown in figure 1 is represented by a special case of (2.10). Letting $\tilde{\delta}_A, \tilde{\delta}_B \rightarrow 0$ in (2.10) recovers the uniform-amplitude inviscid solution of the non-dissipative ($\delta_A, \delta_B = 0$) version of (2.7).

To determine the linearized stability of the solution of (2.7) in (2.10) with or without dissipation, linearize (2.7) about (2.10) by substituting a perturbed solution

$$\left. \begin{aligned} A(X) &= \psi_A(X)[|A_0| + u + iv], \\ B(X) &= \psi_B(X)[|B_0| + w + iz], \end{aligned} \right\} \quad (2.11)$$

where $\{u, v, w, z\}$ are small compared to $|A_0|$ and $|B_0|$. In doing so, one obtains four coupled linear homogeneous partial differential equations for the real and imaginary parts of the perturbations $\{u, v, w, z\}$, each of which depends on $(X, Y, T; \sigma)$. The coefficients in these equations are real, independent of (T, Y) and depend explicitly on X . So, we look for solutions of the form

$$\left. \begin{aligned} u(X, Y, T; \sigma) &= U(X; p, q) \exp[ipT + iqY] + \text{c.c.}, \\ v(X, Y, T; \sigma) &= V(X; p, q) \exp[ipT + iqY] + \text{c.c.}, \\ w(X, Y, T; \sigma) &= W(X; p, q) \exp[ipT + iqY] + \text{c.c.}, \\ z(X, Y, T; \sigma) &= Z(X; p, q) \exp[ipT + iqY] + \text{c.c.}, \end{aligned} \right\} \quad (2.12)$$

where c.c. indicates complex conjugate, p is a real wave frequency, q is a real wavenumber in a Fourier representation and $\{U, V, W, Z\}$ are complex functions of X that satisfy

$$\left. \begin{aligned} c_A \frac{dU}{dX} + i\rho_A U &= \sigma r_A V, \\ c_A \frac{dV}{dX} + i\rho_A V &= \sigma(-r_A + 2\xi_A e^{-2\sigma\tilde{\delta}_A X} |A_0|^2)U + 2\sigma\zeta_{AB} e^{-2\sigma\tilde{\delta}_B X} |A_0||B_0|W, \\ c_B \frac{dW}{dX} + i\rho_B W &= \sigma r_B Z, \\ c_B \frac{dZ}{dX} + i\rho_B Z &= \sigma(-r_B + 2\xi_B e^{-2\sigma\tilde{\delta}_B X} |B_0|^2)W + 2\sigma\zeta_{BA} e^{-2\sigma\tilde{\delta}_A X} |A_0||B_0|U, \end{aligned} \right\} \quad (2.13)$$

in which $\rho_A = p + d_A q$, $\rho_B = p + d_B q$, $r_A = \tilde{\alpha}_A p^2 + \tilde{\gamma}_A p q + \tilde{\beta}_A q^2$ and $r_B = \tilde{\alpha}_B p^2 + \tilde{\gamma}_B p q + \tilde{\beta}_B q^2$. These ordinary differential equations (ODEs) reduce to algebraic equations if there is no dissipation, as in Roskes (1976), Dhar & Das (1991), Ioualalen & Kharif (1994), Baludin *et al.* (1995), Onorato *et al.* (2006) and Shukla *et al.* (2006). Craig *et al.* (2007) analysed both the cases without dissipation, where (2.13) reduce to algebraic equations, and the case with dissipation, where (2.13) remain ODEs.

The essential difference between the two models, with and without dissipation, appears right here. As discussed in detail by Segur *et al.* (2005), dissipation weakens both the perturbation and the carrier wave (as shown by the exponentially decaying coefficients in (2.4), (2.7) and (2.13)). The maximal growth rate of any modulational instability is proportional to the square of the amplitude of the carrier wave, so that the carrier-wave amplitude decays from dissipation, the (X -dependent) growth rates of perturbations become slow and eventually stop. This way the dissipative model predicts linear stability, because the overall growth of any perturbation is bounded.

This argument was carried out in detail by Craig *et al.* (2007), who proved that for $(\tilde{\delta}_A, \tilde{\delta}_B) > 0$ and any choice of the other coefficients in (2.7), the spatially uniform solution (2.10) is linearly stable. (This result similarly holds if T is the evolution variable, instead of X . In that case, one begins with (2.4) instead of (2.7), and then reproduces the steps in (2.8)–(2.13), but with the roles of $\{X, T\}$ interchanged.) In their proof it is essential to use the definition of stability in the sense of Lyapunov (e.g. Nemytskii & Stepanov 1960). In the present context, the solution of (2.7) given in (2.10) is said to be ‘linearly stable’ in the sense of Lyapunov if for every $\epsilon > 0$ there is a $\Delta > 0$ such that if

$$\int \int [u^2 + v^2 + w^2 + z^2] dT dY < \Delta \quad \text{at} \quad X = 0, \quad (2.14a)$$

then

$$\int \int [u^2 + v^2 + w^2 + z^2] dT dY < \epsilon \quad \text{for all} \quad X > 0. \quad (2.14b)$$

Conversely, the solution in (2.10) is ‘linearly unstable’ if there is an $\epsilon > 0$ for which no $\Delta > 0$ satisfies (2.14). In words, stability in the sense of Lyapunov guarantees that any perturbation that starts small enough ($< \Delta$) at $X = 0$ necessarily remains small ($< \epsilon$) for all $X > 0$. This kind of neutral stability is appropriate for Hamiltonian systems (where asymptotic stability is usually impossible), particularly for Hamiltonian evolution equations with variable coefficients for which growth rates are time dependent, like the equations in (2.7) or (2.13).

To obtain the non-dissipative VNLS model, one simply sets $\tilde{\delta}_A = \tilde{\delta}_B = 0$ in (2.4), (2.7) or (2.13). Then (2.13) has constant coefficients, so one may seek exponential solutions. As shown by the authors listed under (2.12), the constant-coefficient version of (2.13) admits exponentially growing solutions for many choices of the coefficients in (2.13); so the non-dissipative VNLS model predicts linear instability of the wave pattern corresponding to (2.1). To compare this prediction with data measured in a dissipative environment, a standard correction (e.g. Benjamin 1967) is to replace the predicted growth rate of the instability with

$$\text{predicted growth rate} - \text{observed decay rate}. \quad (2.15)$$

Then one asserts that the non-dissipative limit of the solution in (2.10) is linearly unstable if there is a perturbation for which

$$\text{predicted growth rate} - \text{observed decay rate} > 0.$$

In what follows, we compare the predictions (from (i) dissipative VNLS and (ii) non-dissipative VNLS with a dissipative correction analogous to (2.15)) with the measured evolution of wave patterns in the following way. For either model, we consider perturbations of the two-dimensional wave pattern in (2.1) or (2.10) that are linearly unstable according to the non-dissipative VNLS model.

(i) For the dissipative VNLS model, we integrate ODEs obtained from (2.13) numerically, using measured initial data in order to include the (important) effects of initial phases in the prediction of the observed evolution of those perturbations.

(ii) For the non-dissipative VNLS model, we follow the same procedure but with $\tilde{\delta}_A = \tilde{\delta}_B = 0$.

In both cases, we amplify the measured amplitudes by $e^{\sigma^2 \tilde{\delta}_A x} = e^{\sigma^2 \tilde{\delta}_B x}$ to compare the measured evolution of the perturbations with that predicted by the two theories. This amplification is used in figures 4–7 and 10. For the dissipative VNLS model, the amplification corresponds to the change of variables in (2.6). For the non-dissipative VNLS model, it provides the *a posteriori* correction for wave damping, discussed above.

2.2. Modelling for symmetric experiments

The experiments described in §3 and presented in §4 use symmetric carrier waves, so that the pattern propagates only in the x -direction and

$$\left. \begin{aligned} k_A = k_B = k, & \quad l_A = -l_B = l, & \quad c_A = c_B = c, \\ d_A = -d_B = d, & \quad |A_0| = |B_0|, & \quad \tilde{\delta}_A = \tilde{\delta}_B = \delta, \\ \tilde{\alpha}_A = \tilde{\alpha}_B = \alpha, & \quad \tilde{\beta}_A = \tilde{\beta}_B = \beta, & \quad \tilde{\gamma}_A = -\tilde{\gamma}_B = \gamma, \\ \xi_A = \xi_B = \xi, & \quad \zeta_{AB} = \zeta_{BA} = \zeta. \end{aligned} \right\} \quad (2.16)$$

In this paper we focus on perturbations with no y -dependence; so $p \neq 0$ and $q = 0$. As discussed by Ioualalen & Kharif (1994), Baludin *et al.* (1995) and others, in the absence of dissipation there are instabilities both with $q = 0$ and with $q \neq 0$. In contrast, Craig *et al.* (2007) predicted linear stability in the presence of damping both with $q = 0$ and with $q \neq 0$. Thus, the conflicting predictions of stability/instability that motivated this experimental study, based on dissipation versus no dissipation, occur both with $q = 0$ and with $q \neq 0$. We consider only y -independent perturbations ($q = 0$) herein because these waves have the spatial periodicity required to fit into our wave tank.

With $p \neq 0$, $q = 0$, the coefficients in (2.13) become

$$\rho_A = \rho_B = \rho = p, \quad r_a = r_b = r = \alpha p^2. \quad (2.17)$$

Then in (2.13) we can make a change of variables that is equivalent to changing to a travelling reference frame for scalar NLS, by defining

$$\chi = \frac{\sigma X}{c} = \frac{\sigma^2 x}{c}. \quad (2.18)$$

This change of variables scales the factor σ out of the evolution equations, as predicted above.

We rewrite the perturbation Fourier amplitudes of $\{u, v, w, z\}$, expressed in (2.12), as

$$\left. \begin{aligned} U(X; p, 0) &= \tilde{U}(\chi) e^{-ipX/c}, \\ V(X; p, 0) &= \tilde{V}(\chi) e^{-ipX/c}, \\ W(X; p, 0) &= \tilde{W}(\chi) e^{-ipX/c}, \\ Z(X; p, 0) &= \tilde{Z}(\chi) e^{-ipX/c}. \end{aligned} \right\} \quad (2.19)$$

(We note that since $X = \sigma x$, the measured perturbation frequency corresponds to σp , so that specifying the value of σ is not required.) With a further change of

variables

$$\left. \begin{aligned} S_1(\chi) &= \frac{\tilde{U}(\chi) + \tilde{W}(\chi)}{2}, & D_1(\chi) &= \frac{\tilde{U}(\chi) - \tilde{W}(\chi)}{2}, \\ S_2(\chi) &= \frac{\tilde{V}(\chi) + \tilde{Z}(\chi)}{2}, & D_2(\chi) &= \frac{\tilde{V}(\chi) - \tilde{Z}(\chi)}{2}, \end{aligned} \right\} \quad (2.20)$$

(2.13) reduces to two uncoupled systems:

$$\left. \begin{aligned} \frac{dS_1}{d\chi} &= rS_2, \\ \frac{dS_2}{d\chi} &= (-r + 2(\xi + \zeta)e^{-2\delta c\chi}|A_0|^2)S_1, \\ \frac{dD_1}{d\chi} &= rD_2, \\ \frac{dD_2}{d\chi} &= (-r + 2(\xi - \zeta)e^{-2\delta c\chi}|A_0|^2)D_1. \end{aligned} \right\} \quad (2.21)$$

It is (2.21) that we integrate numerically to compare predictions and measurements of sideband amplitudes in §4.1.1.

Consistent with (2.1), the water surface can be represented as

$$\begin{aligned} \eta(x, y, t, X, Y, T; \sigma) &= -i\sigma e^{-\delta c\chi} [e^{i\Phi} e^{i(y+\phi_1+\phi_2)} \{|A_0| + u + iv\} - \text{c.c.}] \\ &\quad - i\sigma e^{-\delta c\chi} [e^{i\Phi} e^{i(-ly+\phi_1-\phi_2)} \{|A_0| + w + iz\} - \text{c.c.}] + O(\sigma^2), \end{aligned} \quad (2.22)$$

where

$$i\Phi = i(kx - \omega t) + i\frac{\xi + \zeta}{2\delta c}|A_0|^2(1 - e^{-2\delta c\chi}). \quad (2.23)$$

To obtain initial conditions for $\{S_1, S_2, D_1, D_2\}$ and compare the computed $\{S_1, S_2, D_1, D_2\}$ with subsequent measurements, we relate (2.22) and (2.20) to an expression for the free surface in terms of the Fourier transforms of the measurements:

$$\begin{aligned} \eta(x, y, t) &= \alpha_0 \cos \omega t + \beta_0 \sin \omega t + \alpha_{-1} \cos(\omega - \sigma p)t \\ &\quad + \beta_{-1} \sin(\omega - \sigma p)t + \alpha_1 \cos(\omega + \sigma p)t + \beta_1 \sin(\omega + \sigma p)t. \end{aligned} \quad (2.24)$$

Then $a_0 = \alpha_0 + i\beta_0$, $a_{-1} = \alpha_{-1} + i\beta_{-1}$ and $a_1 = \alpha_1 + i\beta_1$ are the complex Fourier amplitudes corresponding to the carrier wave, the lower sideband and the upper sideband frequencies. The six coefficients on the right-hand side of (2.24) depend only on (x, y) , so they are constants at each measuring site.

Using (2.12) and (2.18)–(2.20), we can also rewrite (2.22) as the sum of three terms, each of which oscillates in time with one of the frequencies $\{\omega, \omega - \sigma p, \omega + \sigma p\}$. After some algebra, aligning the rewritten version of (2.22) with (2.24) determines the coefficients in (2.24) in terms of the variables built into (2.22):

$$\left. \begin{aligned} \alpha_0(x, y) &= 4\sigma e^{-\delta c\chi}|A_0| \cos(ly + \phi_2) \sin\{\Phi|_{t=0} + \phi_1\}, \\ \beta_0(x, y) &= -4\sigma e^{-\delta c\chi}|A_0| \cos(ly + \phi_2) \cos\{\Phi|_{t=0} + \phi_1\}, \\ a_0(x, y) &= \alpha_0 + i\beta_0 = -4i\sigma e^{-\delta c\chi}|A_0| \cos(ly + \phi_2) \exp\{i(\Phi|_{t=0} + \phi_1)\}, \end{aligned} \right\} \quad (2.25)$$

$$\left. \begin{aligned}
 \alpha_{-1}(x, y) &= 4\sigma e^{-\delta c x} |Q(\chi, y)| \sin \left\{ \Phi|_{t=0} + \phi_1 - \frac{pX}{c} + \arg(Q) \right\}, \\
 \beta_{-1}(x, y) &= -4\sigma e^{-\delta c x} |Q(\chi, y)| \cos \left\{ \Phi|_{t=0} + \phi_1 - \frac{pX}{c} + \arg(Q) \right\}, \\
 a_{-1}(x, y) &= \alpha_{-1} + i\beta_{-1} = -4i\sigma e^{-\delta c x} Q(\chi, y) \exp \left\{ i \left(\Phi|_{t=0} + \phi_1 - \frac{pX}{c} \right) \right\},
 \end{aligned} \right\}$$

$$\left. \begin{aligned}
 \alpha_1(x, y) &= 4\sigma e^{-\delta c x} |R^*(\chi, y)| \sin \left\{ \Phi|_{t=0} + \phi_1 + \frac{pX}{c} + \arg(R^*) \right\}, \\
 \beta_1(x, y) &= -4\sigma e^{-\delta c x} |R^*(\chi, y)| \cos \left\{ \Phi|_{t=0} + \phi_1 + \frac{pX}{c} + \arg(R^*) \right\}, \\
 a_1(x, y) &= \alpha_1 + i\beta_1 = -4i\sigma e^{-\delta c x} R^*(\chi, y) \exp \left\{ i \left(\Phi|_{t=0} + \phi_1 + \frac{pX}{c} \right) \right\},
 \end{aligned} \right\}$$

where

$$\left. \begin{aligned}
 Q(\chi, y) &= \{S_1(\chi) + iS_2(\chi)\} \cos(l y + \phi_2) + i\{D_1(\chi) + iD_2(\chi)\} \sin(l y + \phi_2), \\
 R^*(\chi, y) &= \{S_1^*(\chi) + iS_2^*(\chi)\} \cos(l y + \phi_2) + i\{D_1^*(\chi) + iD_2^*(\chi)\} \sin(l y + \phi_2),
 \end{aligned} \right\} \quad (2.26)$$

and (*) denotes complex conjugate. We note that we revert to the original laboratory variables by using $\chi = \sigma^2 x$ and $X = \sigma x$. The value of σ does not have to be specified; it is absorbed in the damping rates, measured amplitudes and perturbation frequency, as shown in §4, Appendix B and also discussed below (2.19).

Next we show that initial measurements of $\{a_0, a_{-1}, a_1\}$ at $x=0$ provide the initial data needed to integrate (2.21). Then the solutions of (2.21) that evolve from these initial data predict measured values of $\{a_0, a_{-1}, a_1\}$ at any $x > 0$. This procedure applies for either the dissipative VNLS model (with $\delta > 0$ in (2.21), (2.22) and (2.25)) or the non-dissipative VNLS model (letting $\delta \rightarrow 0$ in these equations). This way, predictions from each model can be tested experimentally, as we do in §§3 and 4. The *a posteriori* dissipative correction for the non-dissipative model (2.15) amounts to removing the observed decay of the signal by augmenting measured values of the Fourier coefficients by $e^{+\delta c x} = e^{\sigma^2 \delta c x}$ for $x > 0$.

Let $x=0$ denote the location of the first measuring station; then $X=0$, $\chi=0$ and $\Phi|_{t=0}=0$. First consider the carrier wave, which oscillates with frequency ω . From (2.25), at $x=0$,

$$a_0(0, y) = \alpha_0 + i\beta_0 = -4i\sigma |A_0| \cos(l y + \phi_2) \exp\{i\phi_1\}, \quad (2.27)$$

and for $x \geq 0$,

$$|a_0(x, y)| = 4\sigma e^{-\delta c x} |A_0| |\cos(l y + \phi_2)|. \quad (2.28)$$

It follows from (2.28) that a_0 , the amplitude of the carrier-wave pattern, vanishes along nodal lines defined by

$$l y + \phi_2 = \frac{\pi}{2} + m\pi, \quad (2.29)$$

for integer m . Nodal lines of the carrier-wave pattern are evident in figure 1: they are the straight lines, leading away from the paddles, along which the surface remains horizontal. If $\{l\}$ is known, then (2.29) determines ϕ_2 up to a multiple of π . Separately, at an antinode of the carrier wave, y_a , where $\cos(l y_a + \phi_2) = \pm 1$, (2.27) shows that

$$\left. \begin{aligned}
 4\sigma |A_0| &= |a_0(0, y_a)|, \\
 \phi_1 &= \arg\{a_0(0, y)\} \pm \frac{\pi}{2},
 \end{aligned} \right\} \quad (2.30)$$

depending on whether $\cos(l y_a + \phi_2) = \pm 1$. Either choice of signs will do, but then one must maintain that choice throughout the analysis. Equations (2.29) and (2.30) contain the information available from $a_0(0, y)$.

Consider next $a_{-1}(0, y)$ and $a_1(0, y)$. From (2.25), at $x = 0$,

$$\left. \begin{aligned} a_{-1}(0, y) &= \alpha_{-1} + i\beta_{-1} = -4i\sigma Q(0, y)e^{i\phi_1}, \\ a_1(0, y) &= \alpha_1 + i\beta_1 = -4i\sigma R^*(0, y)e^{i\phi_1}, \end{aligned} \right\} \quad (2.31)$$

where $Q(\chi, y)$ and $R^*(\chi, y)$ are defined in (2.26). Evaluate these first at a node of the carrier wave, y_n , where $\cos(l y_n + \phi_2) = 0$ and $\sin(l y_n + \phi_2) = \pm 1$. From (2.26) and (2.31),

$$\left. \begin{aligned} e^{-i\phi_1} a_{-1}(0, y_n) &= \pm 4\sigma [D_1(0) + iD_2(0)], \\ e^{-i\phi_1} a_1(0, y_n) &= \pm 4\sigma [D_1^*(0) + iD_2^*(0)]. \end{aligned} \right\} \quad (2.32)$$

It follows from (2.32) that

$$\left. \begin{aligned} 8\sigma \operatorname{Re}\{D_1(0)\} &= \pm \operatorname{Re}\{e^{-i\phi_1} [a_{-1}(0, y_n) + a_1(0, y_n)]\}, \\ 8\sigma \operatorname{Re}\{D_2(0)\} &= \pm \operatorname{Im}\{e^{-i\phi_1} [a_{-1}(0, y_n) + a_1(0, y_n)]\}, \\ 8\sigma \operatorname{Im}\{D_1(0)\} &= \pm \operatorname{Im}\{e^{-i\phi_1} [a_{-1}(0, y_n) - a_1(0, y_n)]\}, \\ 8\sigma \operatorname{Im}\{D_2(0)\} &= \mp \operatorname{Re}\{e^{-i\phi_1} [a_{-1}(0, y_n) - a_1(0, y_n)]\}. \end{aligned} \right\} \quad (2.33)$$

Equations (2.33) provide the initial data required for the D -equations in (2.21).

Now evaluate (2.31) at $x = 0$ and at an antinode of the carrier wave, where $\cos(l y_a + \phi_2) = \pm 1$ and $\sin(l y_a + \phi_2) = 0$. One shows from (2.26) and (2.31) that

$$\left. \begin{aligned} 8\sigma \operatorname{Re}\{S_1(0)\} &= \pm \operatorname{Im}\{e^{-i\phi_1} [a_{-1}(0, y_a) + a_1(0, y_a)]\}, \\ 8\sigma \operatorname{Re}\{S_2(0)\} &= \pm \operatorname{Re}\{e^{-i\phi_1} [a_{-1}(0, y_a) + a_1(0, y_a)]\}, \\ 8\sigma \operatorname{Im}\{S_1(0)\} &= \pm \operatorname{Re}\{e^{-i\phi_1} [a_{-1}(0, y_a) - a_1(0, y_a)]\}, \\ 8\sigma \operatorname{Im}\{S_2(0)\} &= \mp \operatorname{Im}\{e^{-i\phi_1} [a_{-1}(0, y_a) - a_1(0, y_a)]\}. \end{aligned} \right\} \quad (2.34)$$

Given these initial data, one can integrate (2.21) to obtain $\{S_1(\chi), S_2(\chi), D_1(\chi), D_2(\chi)\}$ for any $\chi > 0$. Then (2.25) and (2.26) predict the values of the Fourier coefficients of the carrier-wave pattern and the two excited sidebands at any desired (x, y) .

Note that the formulae in (2.33) and (2.34) are relatively simple because we restricted our attention to perturbations that are y -independent (so $q = 0$ in (2.12)). For y -independent perturbations, the Fourier coefficients in (2.25) inherit the y -periodicity of the carrier wave; so they must satisfy the following consistency conditions. For any $x \geq 0$ and any (y) for which $(y \pm \pi/l)$ lies within the test section of the experiment,

$$\left. \begin{aligned} a_0(x, y) &= -a_0(x, y \pm \pi/l), \\ a_{-1}(x, y) &= -a_{-1}(x, y \pm \pi/l), \\ a_1(x, y) &= -a_1(x, y \pm \pi/l). \end{aligned} \right\} \quad (2.35)$$

If the measured values of these Fourier coefficients at $x = 0$ fail these consistency conditions, then either the imposed perturbations are not y -independent or some other assumption implicit in this analysis is not satisfied.

Finally, we note that the differential equations in (2.21) decouple in S and D because the carrier-wave pattern is symmetric and the water is deep. This symmetry in deep water results in a pattern whose contours are rectangular, rather than hexagonal as they are for patterns in shallow water (e.g. Hammack, Scheffner & Segur 1989). Symmetric patterns on deep water exhibit nodal lines (i.e. lines in x with no surface

Experiment	H^p (cm)	H_3^p (cm)	$\omega_p/(2\pi)$ (s $^{-1}$)	a_p	Surface	Water	$\sigma^2\delta$ (m $^{-1}$)
1M	0.6	−0.10	0.571	0.050	2 h + oil	1 day	0.248
2M	0.6	−0.10	0.571	0.050	2 days	2 days	0.378
3M	0.5	−0.05	0.571	0.042	1 h + oil	1 day	0.310
4M	0.6	−0.10	0.571	0.050	1 h + oil	2 day	0.150
5M	0.5	−0.05	0.571	0.042	1 day	4 days	0.022
6M	0.5	−0.05	0.571	0.042	2 days	2 days	0.150
7M	0.6	−0.10	0.800	0.050	2 days	6 days	0.074
8L	0.6	−0.10	0.571	0.100	1 h	2 h	0.128

TABLE 1. Prescribed experimental parameters for the moderate- (§4.1) and large-amplitude (§4.2) experiments.

displacement), which do not occur in a hexagonal pattern. The existence of nodal lines also provides a reason for the relative simplicity of the formulae in (2.29)–(2.34).

2.3. Numerical considerations

In order to compare predictions from the nonlinear theory with the experimental measurements presented in §4, rewrite (2.7) as

$$ic\tilde{A}_x + \alpha\tilde{A}_{\tau\tau} + e^{-2\sigma^2\delta x}(\xi|\tilde{A}|^2 + \zeta|\tilde{B}|^2)\tilde{A} = 0, \quad (2.36a)$$

$$ic\tilde{B}_x + \alpha\tilde{B}_{\tau\tau} + e^{-2\sigma^2\delta x}(\xi|\tilde{B}|^2 + \zeta|\tilde{A}|^2)\tilde{B} = 0, \quad (2.36b)$$

where we have used the fact that $\partial_y = 0$ for the experiments herein. In (2.36), $\tilde{A} = \sigma A$, $\tilde{B} = \sigma B$, $\tau = t - x/c$ and x and t are the original physical variables. The parameters α , ξ and ζ are constant for all experiments and are given in table 3; $c = 20.95$ cm s $^{-1}$. The values of $\sigma^2\delta$ vary from experiment to experiment and are given in table 1. We consider this system with periodic boundary conditions in the τ dimension and evolve the solution over $x \in [0, 150]$ (in centimetres). For each of the experiments, we used initial conditions of the form

$$A(x = 0, \tau) = -ie^{i\phi_1}(A_0 + ((D_1(0) + S_1(0))e^{3.588i\tau} + \text{c.c.}) + i((D_2(0) + S_2(0))e^{3.588i\tau} + \text{c.c.})), \quad (2.37a)$$

$$B(x = 0, \tau) = ie^{i\phi_1}(A_0 + ((-D_1(0) + S_1(0))e^{3.588i\tau} + \text{c.c.}) + i((-D_2(0) + S_2(0))e^{3.588i\tau} + \text{c.c.})), \quad (2.37b)$$

where A_0 and ϕ_1 are given in table 2, and $S_1(0)$, $S_2(0)$, $D_1(0)$ and $D_2(0)$ are given in tables 6 and 7 in Appendix B.

For the non-dissipative case ($\sigma^2\delta = 0$), we used 256 Fourier modes/grid points in the τ dimension. For the dissipative case ($\sigma^2\delta > 0$), we used 128 Fourier modes. Fewer modes are required in the dissipative case because higher wavenumber modes do not become excited. The M integral was preserved to at least 10 places and the P_x integral was preserved to at least 6 places for all numerical simulations.

Results from numerical computations are presented in §4.1.2.

3. Experimental apparatus and procedures

Patterns of waves corresponding to interacting wavetrains have been studied experimentally by Kimmoun *et al.* (1999), Hammack *et al.* (2005) and Henderson

et al. (2006). Herein we report on experiments for the special case when the A and B waves are symmetric, as defined by (2.16). The pattern shown in figure 1 was generated in a 6×12 ft² tank with an array of 32 plunger-type paddles with triangular cross-sections (visible at the far end of the tank in figure 1), each individually controlled and together spanning the width $W = 6$ ft (see Hammack *et al.* 2005 for details). The water depth h was 19.5 ± 0.5 cm for the eight experiments discussed herein. Experiments 1M–7M (M for moderate) had ‘small to moderate’ amplitudes, as defined in Segur *et al.* (2005). That is, the data in these experiments conserved P_x in (2.9). Experiment 8L (L for large) had a large (perturbation) amplitude, where, as defined in Segur *et al.* (2005), we take ‘large amplitude’ to mean that the data did not conserve P_x in (2.9).

The pattern in figure 1, which looks similar to those used in all of our experiments, was generated by programming the paddles to oscillate according to

$$\eta_p = H^p \cos\left(\frac{n\pi}{W} y_j\right) \cos(\omega t) + H_3^p \cos\left(\frac{3n\pi}{W} y_j\right) \cos(\omega t), \quad (3.1)$$

where H^p and H_3^p are amplitudes of the paddle motions, which are different from the amplitudes of the water motion. In (3.1) we included a third harmonic term, whose importance was first recognized by Fuhrman & Madsen (2006) and then verified experimentally by Henderson *et al.* (2006). An explicit formula is given in both places. Including this third harmonic term is essential in generating bi-periodic patterns of waves with nearly permanent form. It is not included in the theory (§2), because it is of higher order, $O(\sigma^3)$, than the terms considered there. An explanation of why H_3^p is required for numerical and physical experiments was given by Fuhrman & Madsen (2006). The values of wavemaker displacements, H^p and H_3^p , used in experiments 1M–8L are listed in table 1.

In (3.1), y_j is the digitized y -location of the centre of the $j = 1, \dots, 32$ paddles, x is the distance perpendicular to the paddles, $\omega = 8\pi \text{ s}^{-1} = 4$ Hz is the frequency and $n = 5$ is the number of nodal lines in the tank, which are visible in figure 1.

With a common frequency of 8π , the wave patterns in figure 1 and in all of the experiments presented herein have wavenumbers $\kappa = 0.626 \text{ cm}^{-1}$ and x -wavelengths of about 10 cm. With a water depth of about $h = 20$ cm, $\kappa h > 12$, so that these were deep-water waves. The relative strength of gravity versus surface tension for these waves is measured by the Bond number, $Bo = g/(T\kappa^2) = 981/\{(70)(0.626)^2\} = 36$, so surface tension had a small but measurable effect on the waves. We include surface tension in our calculations.

To study the stability of the wave pattern generated using (3.1), we perturbed it at the wavemakers by multiplying (3.1) by $(1 + a_p \cos(\omega_p t))$, where a_p is the ratio of perturbation and carrier-wave amplitudes and $\omega \pm \omega_p$ are the frequencies of the sideband perturbations of the carrier waves. The experimental perturbation frequency, ω_p , corresponds to σ_p in (2.12) and to b in (2.8b) and (2.9). The values prescribed to the wavemakers in the experiments herein are listed in table 1. As with all of the prescribed paddle motions, the wavemakers’ values of a_p are different from the amplitude ratios of the water motion. The wavemakers’ frequencies are the same as those measured in the water waves.

To obtain a data set corresponding to one of the nine experiments listed in table 1, we conducted five ‘sub-experiments’. That is, we set the wave gauges in position, ran the wavemaker and obtained time series at this fixed position. Then we moved the wave gauges to the next x -location, waited 15 min to obtain quiescent water, ran the wavemaker and obtained time series. We repeated this procedure for a total of five times and place the results from these five sub-experiments together to obtain the data sets for each of the experiments 1M–8L.

We used four *in situ* gauges. One was permanently situated as close as possible to the wave paddles to monitor reproducibility of experiments. The data shown here were obtained from three gauges at x -locations, $x_{i+1} = x_i + 35$ cm, with $i = 1, \dots, 5$, corresponding to each of the five sub-experiments. The y -locations were held constant in each of the five sub-experiments and were at: $y = 0$, corresponding to the nodal line in the centre of the tank (the location of gauge 2); $y = -\pi/(2l)$, corresponding to the antinodal line to the left of the centreline (the location of gauge 1); and $y = \pi/(2l)$, corresponding to the antinodal line to the right of the centreline (the location of gauge 3). The gauges were capacitance-type probes made with a wire in a glass capillary tube sealed at the end and penetrating the water; the water and wire acted as plates of the capacitor, and the glass was the dielectric. They measured the water-surface displacement at a ‘point’ (a circular area of about 1 mm in diameter) with a resolution of ± 0.005 cm. The first measurement station was defined to be at $x_1 = 0$. The physical location of x_1 , relative to the wavemakers, was chosen to be outside the region of evanescent waves near the wavemaker; the last measurement station x_5 was chosen far enough from the end wall that we could record sufficient data at x_5 before the reflected wave corrupted the signal. We note that our data do not quite satisfy the consistency relations (see (2.35)), so we used starting values for (2.21) that made both the dissipative ($\delta \neq 0$) and non-dissipative ($\delta = 0$) versions agree with the data initially (see §4).

The measured damping rate played a crucial role in this study, because we could discriminate between the predictions of the two theoretical models within the (short) test section of our tank only if the damping rates were large enough. Our experience, as reported in Segur *et al.* (2005) and Henderson *et al.* (2006), is that significant dissipation occurs within the boundary layer at the free surface, rather than at the wetted perimeter of the fluid domain. During the course of these experiments, we found that the surface boundary layer has two effects: (i) it causes linear dissipation and (ii) it affects the shape of the initial wave envelopes (the wavefronts); in particular, waves on an untreated surface ramped up to a uniform amplitude over a significant evolution distance. Because of the shortness of our test section, we needed the dissipation rate to be ‘large enough’ and the time series of the (associated unperturbed) waves to have a uniform amplitude as near as possible to the wavemaker. So, in all of our experiments, we cleaned the surface (following Rayleigh 1890) by scraping a brass rod that spanned the tank width over the tank length in one direction. We used a wet-vac to remove the compressed film at one end of the tank. Then we scraped the surface in the opposite direction and vacuumed the film at the other end. Scraping the surface in this way ensured that the time series of the unperturbed waves was uniform at the first gauge site for a few days. However, the damping rate (in combination with the carrier-wave amplitude) was sometimes too small to distinguish between the dissipative and non-dissipative predictions. The damping rate was approximately constant for a few hours (it took 2 h to perform each set of five sub-experiments) but varied with surface age. In previous experiments on one-dimensional waves in a long channel, Segur *et al.* (2005) found that the damping rate increased monotonically with surface age; here the dependence on surface age was not so clearly correlated. However, to increase the damping rate we conducted some of the experiments herein a day or two after cleaning the surface. In other experiments herein, we added a few drops of cooking oil (Smart Balance Omega) to the surface after cleaning it to enhance the damping rate. We note that the experiments with oil had an enhanced damping rate but the waves behaved qualitatively the same as in experiments without oil. The oil acts as a surfactant; a review of surfactant rheology and how it increases the damping rate of water waves is given in Lucassen (1982); experimental investigations

include Davies & Vose (1965), Huhnerfuss, Lange & Walter (1985) and Henderson (1998). Either method (increasing surface age or adding oil) usually gave sufficient dissipation rates, and we consider only those experiments that had uniform envelopes for the (associated unperturbed) waves. We do not yet know what happens at the free surface, but we try to control it by cleaning the surface, letting it age and/or by adding oil. In the end, we take what we get for the dissipation rates. Table 1 lists the surface age after it was cleaned with the brass rod and whether oil was added. It also lists the length of time that the water was in the tank after the entire tank was cleaned (with alcohol) and filled. The measured value of the spatial decay rate, $\sigma^2\delta$, was obtained by fitting an exponential decay curve to measurements of

$$M \exp(-2\sigma^2\delta x) = \int \left(\sum_{j=-N}^N |a_j|^2 \right) dY, \quad (3.2)$$

obtained at each of the x_i . For our Fourier series $N = 11$, and a_j are the 23 Fourier coefficients associated with a frequency band of ± 2 Hz around the carrier wave frequency of 4 Hz. The upper and lower sideband amplitudes, $a_{\pm 1}$, correspond to $j = \pm 3$. The integration in Y was done using the rectangle rule with the three data points obtained from the three gauges at the fixed x_i . The value of δ obtained was then used in computations of P_x . To perform the computations of P_x , we rewrite (2.9) in terms of measurable quantities to obtain

$$P_x = \exp(2\sigma^2\delta x) \frac{1}{b} \int \left(\sum_{j=-N}^N (\omega_j - \omega_0) |a_j|^2 \right) dY, \quad (3.3)$$

using measurements obtained at each of the x_i . In (3.3) $\omega_j - \omega_0$ measures the frequency difference of the j th frequency component from the carrier-wave frequency, $b = 3.588 \text{ s}^{-1}$ is the absolute value of the difference between the sideband frequencies ($j = 3$) and the carrier-wave frequency, and the frequency resolution of the Fourier transforms is $b/3$. We note that the Fourier amplitudes a_j listed here are those measured in the wave tank, so they decay in x ; the conserved quantities M and P_x are in the coordinate system that factors out the decay; thus, if they are conserved as predicted, they remain constant.

4. Results

Here we present results from eight sets of (approximately symmetric) experiments: (i) seven in which both the carrier-wave amplitudes and the perturbation amplitudes were moderate (experiments 1M–7M) and (ii) one in which the perturbation amplitude was large (experiment 8L). Table 2 lists measurements of the carrier-wave amplitudes and phases from the Fourier transforms taken at the first measurement site, and the measured dissipation rates obtained as described in §3 for each of the eight sets of experiments.

For two of the sets of experiments, 1M and 8L, we show time series from the three gauges at the five measurement sites, the Fourier transforms of the time series and measurements of the conserved quantities (2.8). For all of the moderate-amplitude experiments, 1M–7M, we show predictions and measurements of the evolution of the sideband Fourier amplitudes, because the evolution of these sidebands determines whether the carrier-wave pattern is linearly unstable or stable. Predictions are shown

Expt no.	$ a_0 $ (cm) (gauge 1)	$ a_0 $ (cm) (gauge 3)	$\arg(a_0)$ (rad) (gauge 1)	$\arg(a_0)$ (rad) (gauge 1)	$\sigma^2\delta$ (m ⁻¹)	σA_0	ϕ_1
1M	0.372	0.336	0.749	-1.912	0.248	0.093	-4.472
2M	0.397	0.413	-2.738	1.084	0.378	0.099	-1.571
3M	0.303	0.264	2.140	-0.429	0.310	0.076	-4.426
4M	0.349	0.354	-2.518	-0.110	0.150	0.089	-2.775
5M	0.386	0.409	-1.223	2.413	0.022	0.102	-2.793
6M	0.412	0.436	-2.328	1.198	0.150	0.109	-0.373
7M	0.357	0.356	-0.826	2.421	0.074	0.089	0.845
8L	0.413	0.380	0.398	-2.699	0.128	—	—

TABLE 2. Measured values of the amplitudes and phases of the carrier-wave patterns, the damping rates obtained from (3.2) and values of coefficients associated with the carrier-wave patterns that are used for numerical integrations of (2.21).

both from the linearized stability theories (dissipative and non-dissipative) and from computations of the nonlinear theories (dissipative and non-dissipative).

4.1. Moderate-amplitude experiments

Figure 2 shows the time series from the three gauges at x_i $\{i = 1, \dots, 5\}$ in experiment 1M. The perturbation grew during this interval – one sees the growth of the sidebands and the loss of energy of the carrier wave (due to both viscous decay and nonlinear interactions) in the corresponding Fourier transforms shown in figure 3.

Figure 4(a) shows measurements of M obtained from (3.2) using $\sigma^2\delta = 0.248$ m⁻¹, which was chosen to make the measurements as nearly constant as possible. Recall that M factors out exponential decay and is predicted to be constant by (2.7). The fact that we were able to find a value of $\sigma^2\delta$ that caused the computed values of M to be nearly constant confirms that the data decay nearly exponentially. The non-dissipative theory (2.2) also has an associated M -type integral that is $M \exp(-2\sigma^2\delta x)$. So, the measured values of M shown in figure 4(a) also correspond to an *a posteriori* correction of the non-dissipative M -type integral.

Figure 4(b) shows measurements of P_x obtained from (3.3), using the value of $\sigma^2\delta$ obtained from figure 4(a). Recall that the dissipative theory (2.7) predicts that if the waves are decaying at a rate given by $\sigma^2\delta$ then P_x , which factors out the exponential decay, will be constant. The fact that these data are indeed nearly constant (essentially zero) is then a non-trivial test of the theory. As with M , the non-dissipative theory (2.2) also has an associated P_x -type integral that is $P_x \exp(-2\sigma^2\delta x)$. So, the measured values of P_x shown in figure 4(b) also correspond to an *a posteriori* correction of the non-dissipative P_x -type integral.

We consider the conservation or non-conservation of P_x to be a fundamental result that provides a diagnostic of whether or not the NLS-type theories are valid for the wavefield under consideration: if the measurements of P_x are not conserved, then neither dissipative nor non-dissipative NLS-type theories are appropriate. Further, in our experiments for which measurements of P_x are not conserved (see §4.2) there is always an associated shift of the energy peak in the spectrum from the carrier-wave frequency to its lower sideband. Indeed, one can consider the ratio P_x/M to be an average wave frequency (see Gordon 1986), which would be a constant if both P_x and M are conserved. Similarly, in the non-dissipative theory, the analogous ratio would be a constant if both the M -type integral and P_x -type integral decayed at the same rate. Thus, we also consider the downshifting identified by a monotonic decrease in

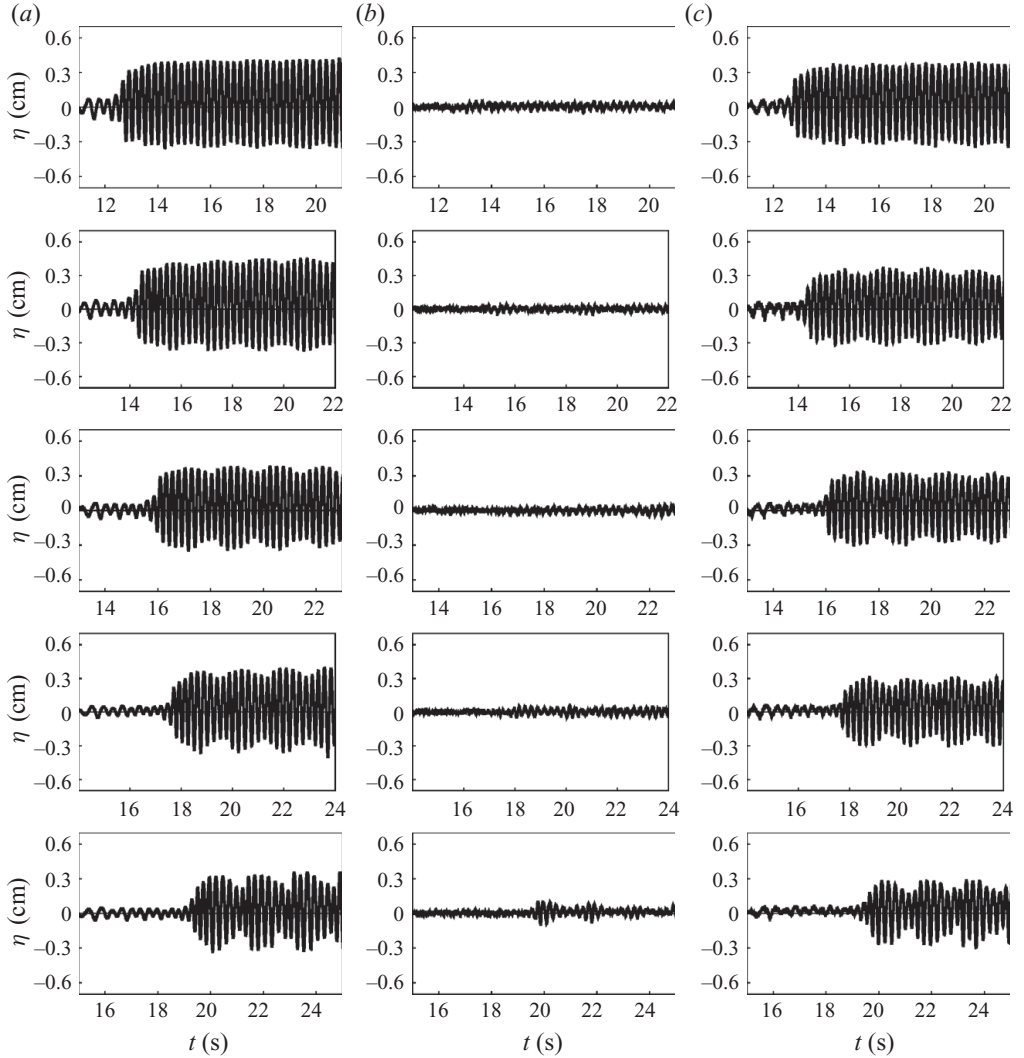


FIGURE 2. Experiment 1M. Water-surface displacement as a function of time for gauges in the (nodal) centreline of the tank (b) and in the centre of the antinodal regions on its left side (a) and right side (c) at the five measuring stations, which were 35 cm apart.

P_x to be a diagnostic for the validity of NLS-type theories: if downshifting occurs, then neither dissipative nor non-dissipative NLS-type theories are appropriate. Note that in figure 3 the peak of the spectrum remains at the carrier-wave frequency of 4 Hz for all x , consistent with the conservation of P_x in this experiment.

4.1.1. Comparison of measurements and predictions from linear stability theory

We used Mathematica to compute numerical solutions to the ODEs (2.21). Table 3 lists the frequencies and number of nodal lines n in the wave patterns as well as the associated coefficients that are used in the computations. The y -wavenumber, $l = n\pi/W$, and the x -wavenumber, k , are obtained from the linear dispersion relation, $\omega^2 = g\kappa + T\kappa^3$, where $\kappa^2 = k^2 + l^2$, g is the acceleration of gravity and $T = 70 \text{ dyn cm}^{-1}$

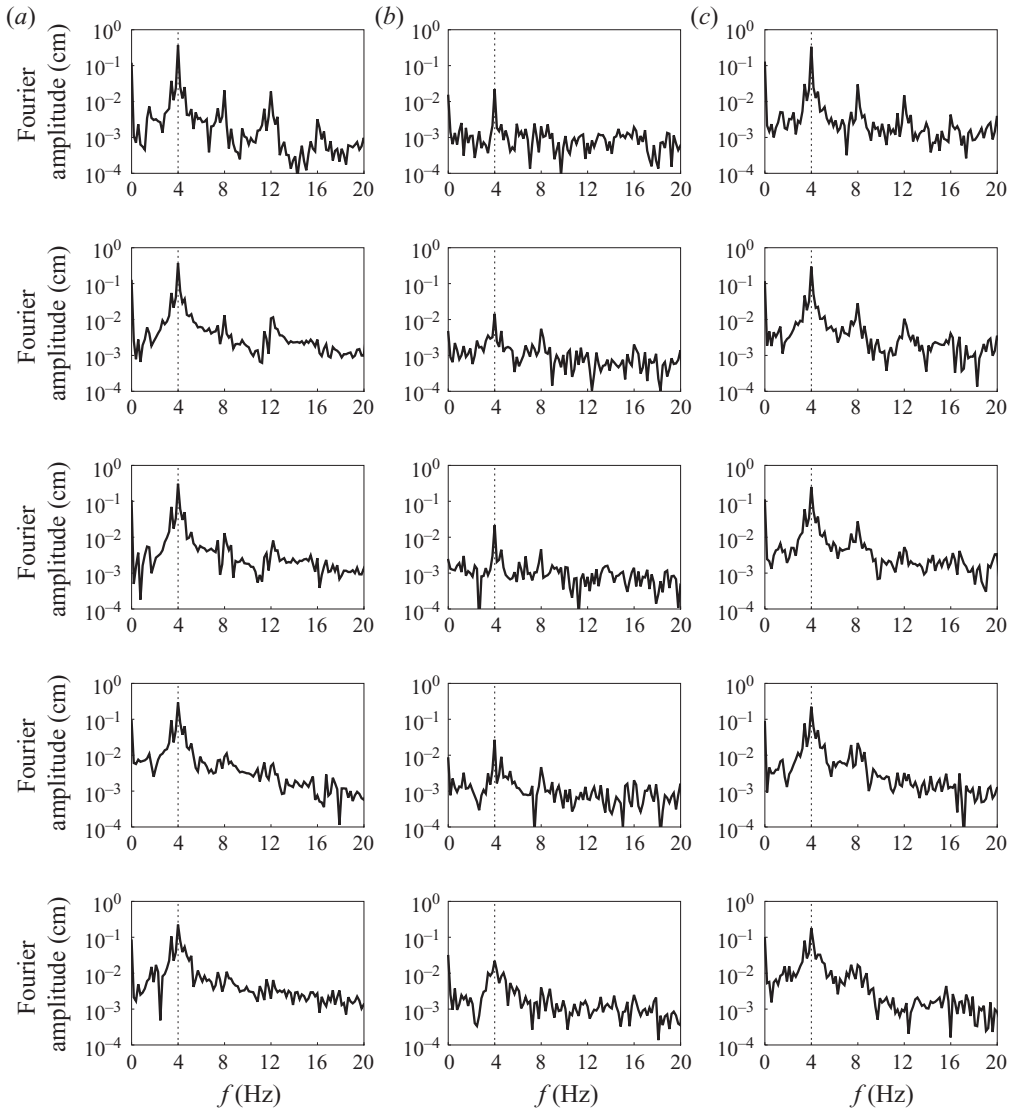


FIGURE 3. Experiment 1M. Fourier transforms of the data shown in figure 2 with respect to cyclic frequency f . The dashed vertical line is at the carrier-wave frequency $f = \omega/2\pi = 4$ Hz.

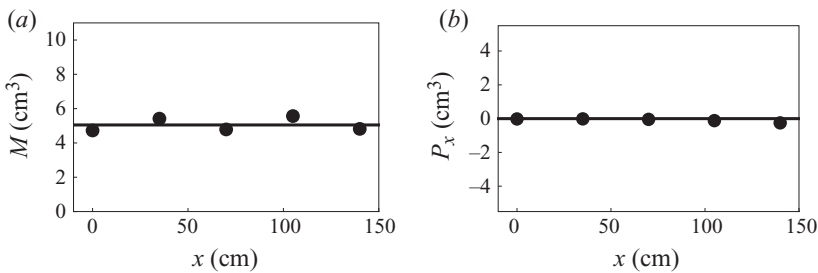


FIGURE 4. Experiment 1M. Measurements (dots) of (a) M and (b) P_x using $\sigma^2\delta = 0.248 \text{ m}^{-1}$. The horizontal lines are drawn arbitrarily as reference to show constant values.

ω (s ⁻¹)	n	α (s)	β (cm ² s ⁻¹)	γ (cm)	ξ (cm ² s) ⁻¹	ζ (cm ² s) ⁻¹
8π	5	-0.013	17.181	0.223	-20.396	-38.393

TABLE 3. Frequency of the carrier-wave pattern, span-wise mode number and numerical values for the coefficients defined in (2.16) in terms of coefficients first used in (2.7).

Expt no.	$ a_{-1} $ (cm) (gauge 1)	$ a_{-1} $ (cm) (gauge 3)	$\arg(a_{-1})$ (rad) (gauge 1)	$\arg(a_{-1})$ (rad) (gauge 3)
1M	0.038	0.031	0.070	-2.673
2M	0.033	0.033	-1.906	1.682
3M	0.013	0.019	1.211	-1.358
4M	0.022	0.023	2.554	-1.100
5M	0.027	0.026	-1.061	2.349
6M	0.036	0.033	-2.716	0.710
7M	0.029	0.028	-1.155	1.883
8L	0.083	0.072	0.032	3.125

TABLE 4. Initial amplitudes and phases of the lower sidebands.

Expt no.	$ a_1 $ (cm) (gauge 1)	$ a_{-1} $ (cm) (gauge 3)	$\arg(a_1)$ (rad) (gauge 1)	$\arg(a_{-1})$ (rad) (gauge 3)
1M	0.025	0.019	-1.498	2.258
2M	0.023	0.019	-0.209	-2.393
3M	0.007	0.010	0.136	-2.749
4M	0.009	0.013	2.325	-1.798
5M	0.022	0.020	2.097	-0.204
6M	0.024	0.024	1.511	-1.253
7M	0.017	0.014	2.742	-0.152
8L	0.051	0.046	-2.012	1.380

TABLE 5. Initial amplitudes and phases of the upper sidebands.

is the value of the surface tension used. These numbers were the same for all of the experiments.

The values for $|A_0|$, which is a coefficient in (2.21), and ϕ_1 , which is required for the initial conditions, come from the carrier-wave patterns measured at x_1 in each set of experiments. Their values are related to measurements of the complex Fourier amplitude of the carrier-wave frequency by (2.30). However, because the actual wave patterns were not perfectly symmetric, we could not unambiguously use (2.30). Instead, we chose values for $|A_0|$ and ϕ_1 to ensure that the computations of both the dissipative ($\delta \neq 0$) and non-dissipative ($\delta = 0$) versions of (2.21) agreed with the data initially. The values we used are listed in table 2. The initial values for the S and D are listed in Appendix B.

Once the values of $|A_0|$ and ϕ_1 were chosen, there were no further choices. The initial conditions for (2.21) are given by (2.33) and (2.34). The values of $a_{\pm 1}(0, y_n)$ and $a_{\pm 1}(0, y_a)$ are the Fourier amplitudes of the upper and lower sidebands measured at x_1 in each set of experiments. Their magnitudes and phases are listed in tables 4 and 5.

The computations of (2.21) give values of S_i and D_i , $i = 1, 2$, as a function of x . The corresponding amplitudes of the upper and lower sidebands, $a_{\pm 1}$, are related to S_i and D_i by (2.24), (2.25) and (2.26) using $\cos(l y + \phi_2) = 1/0$ to correspond to gauges

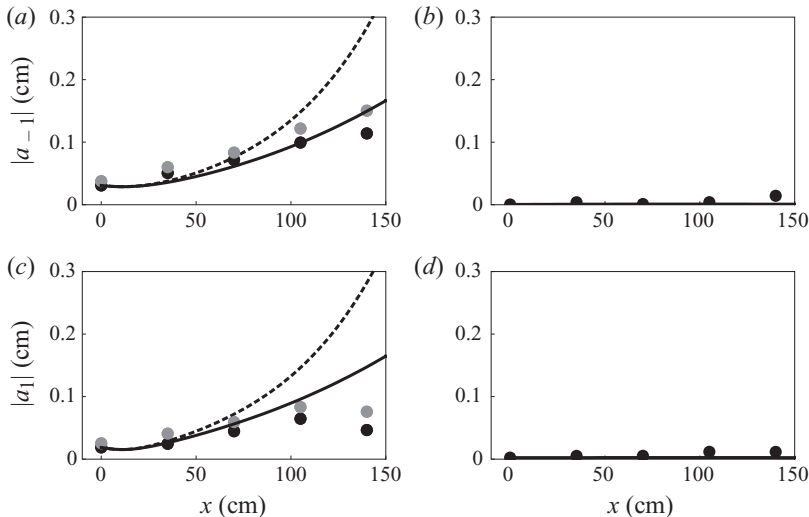


FIGURE 5. Measurements (dots), multiplied by $e^{\sigma^2 \delta x}$, and predictions (curves) from computations of (2.21) of the amplitudes of the two seeded sidebands from the three gauges. The gauges are in the antinodal region to the left (black) and right (grey) of the centreline (a , c), and in the nodal line (b , d). The solid curves are from the dissipative theory. The dashed curves are from the non-dissipative theory.

in antinodes/nodes. We note that for each experiment one set of initial data gives the predictions of both sidebands.

Figure 5 shows measurements from experiment 1M of the magnitudes of the complex Fourier amplitudes, $a_{\pm 1}$, corresponding to the wave components with frequencies $\omega \pm \omega_p$ obtained by the three gauges at the five measurement stations. For appropriate comparisons with both the dissipative and non-dissipative theoretical predictions we have amplified the measurements by the same exponential as the theory so that the actual values shown are $\exp(\sigma^2 \delta x) |a_{\pm 1}(x, y)|$. Predictions from (2.21), obtained as described above, are also shown for $\delta = 0$ and for $\sigma^2 \delta = 0.248 \text{ m}^{-1}$. Multiplying the data by the exponential factor corresponds to adjusting the non-dissipative theory for dissipative effects *a posteriori* as in (2.15). For the dissipative (δ -VNLS) model, multiplying the data by this factor corresponds to the change of variables in (2.6). Thus, adjusting the data in this way can be interpreted sensibly in either theory, but figures 5(a) and 5(c) show that the two theories give quite different predictions, even over the (relatively short) 140 cm of our test section. The x -interval of 140 cm over which measurements were obtained corresponds to about 14 wavelengths of the 4 Hz carrier waves. Figure 5(a) shows that the growth of the lower sideband, $|a_{-1}|$, is well modelled by the dissipative (δ -VNLS) theory, much more accurately than the non-dissipative theory. Figure 5(c) shows that the upper sideband, $|a_{1}|$, is modelled better by the dissipative theory than by the non-dissipative theory, but both theories over-predict the growth of the upper sideband. Figures 5(b) and 5(d) show that the nodal lines remain quiescent, as predicted by both models, even as perturbations grow in the antinodal regions. Having the lower sideband grow faster than the upper sideband is typical in experiments like these, not only for bi-periodic waves but also for plane waves (see the data of Lake *et al.* 1977, Melville 1982, Segur *et al.* 2005 and others).

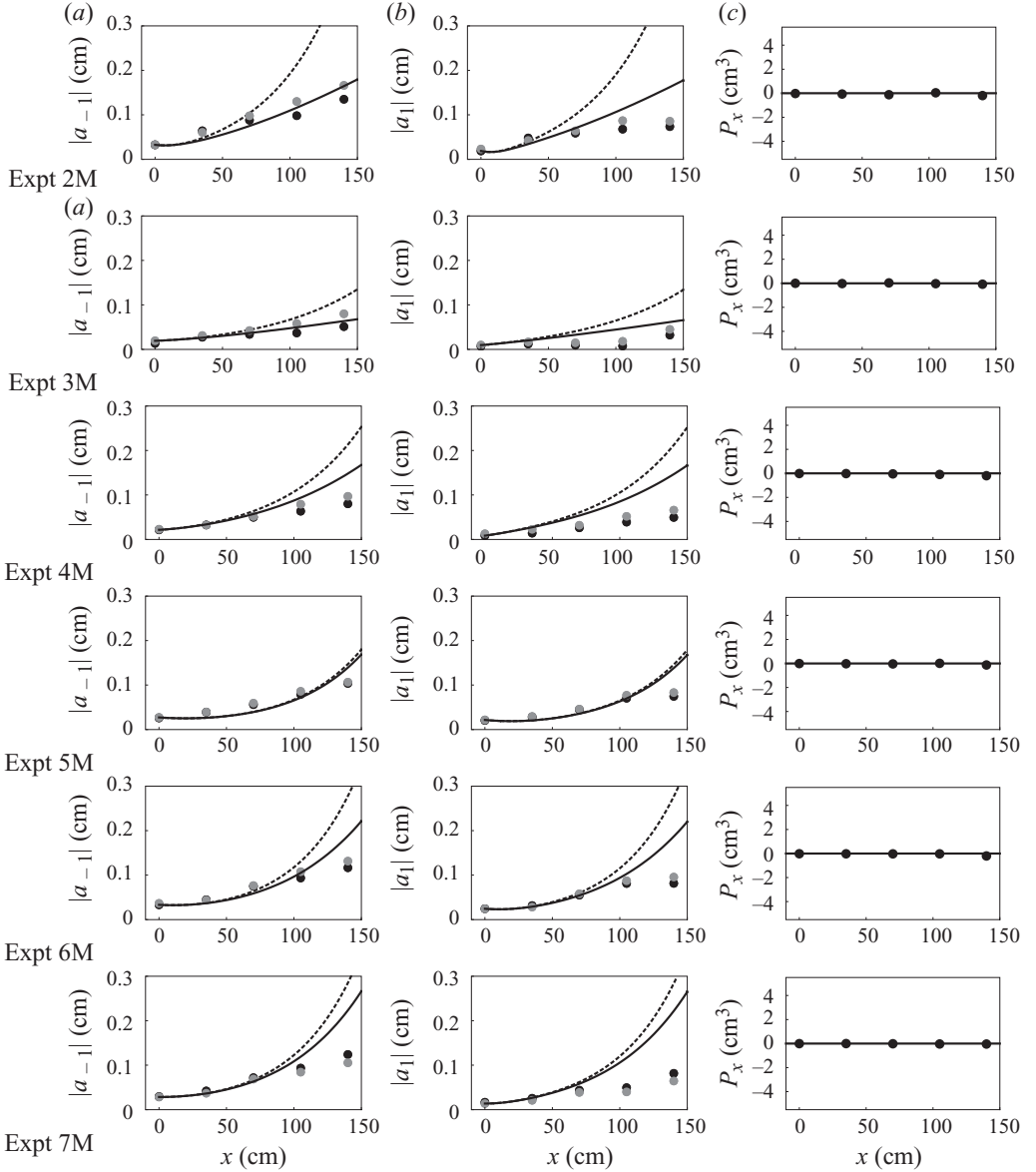


FIGURE 6. Results from experiments 2M–7M. Columns (a) and (b) show measurements (dots), multiplied by $e^{\sigma^2 \delta x}$, and predictions (curves) from computations of (2.21) of the amplitudes of the lower (a) and upper (b) seeded sidebands from the two gauges in the antinodal region to the left (black) and right (grey) of the centreline of the wave tank. The solid curves are from the dissipative theory. The dashed curves are from the non-dissipative theory. Column (c) shows P_x (in the dissipative reference frame). The horizontal lines are drawn arbitrarily as reference to show constant values. The dissipation rate used for each row is listed in table 2 for the corresponding experiment.

There is nothing special about the experiment shown in figures 2–5. Comparisons of measurements (amplified by the exponential factor as in figure 5) and the dissipative/non-dissipative predictions of the sideband amplitudes are shown for six additional experiments in figure 6, along with graphs of the diagnostic P_x given

by (3.3), which use the value of $\sigma^2\delta$ obtained from (3.2). The first column of figure 6 shows comparisons for the lower sideband, $|a_{-1}|$; the second column of figure 6 shows comparisons for the upper sideband, $|a_1|$. The theoretical predictions (with and without dissipation) are the same for each sideband, while in the experiments either $|a_{-1}|$ and $|a_1|$ grew at the same rate or $|a_{-1}|$ grew faster. In all cases the dissipative theory does a better job of predicting measurements than the non-dissipative theory, except perhaps in one case, experiment 5M, in which the two theories were virtually indistinguishable within the 140 cm test section of our tank. Thus, experiments in our (short) tank were able to discriminate between the predictions of the two models tested only for large enough dissipation rates.

The experiments shown in figures 2–5 and figure 6 show: (i) a clear difference in the theories with and without dissipation and (ii) that the dissipative (δ -VNLS) theory models the experiments more accurately than does the non-dissipative theory, even after an *a posteriori* correction for dissipation.

4.1.2. Comparison of nonlinear inviscid and dissipative theories

Separate from the question of linear stability is the question of the effects of nonlinear interactions. Here we show numerical computations (discussed in §2.3) of the nonlinear VNLS equations, (2.7), rewritten as (2.36) with dissipation ($\delta > 0$) and without dissipation ($\delta = 0$). We recall that (2.36) are in the reference frame that factors out dissipation, as described in the last paragraph of §2.1. All of the computations herein used initial conditions corresponding to the experimental values for the associated experiments, experiments 1M–7M.

Figure 7 shows comparisons of the nonlinear results with measurements over the short (about 150 cm) distance available for the physical experiments. Columns (a) and (b) show a comparison of the measured and simulated sideband amplitudes for all seven experiments. (Experiment 1M is shown in the last row of figure 7 for an easier row-by-row comparison with the linear results shown in figure 6. For the linear results, Experiment 1M is shown in figure 5.) In Experiments 1M–4M and 6M, the curves from the dissipative nonlinear theory are essentially identical to the curves from the dissipative linear theory shown in figures 5 and 6. For these experiments the curves from the non-dissipative nonlinear theory are qualitatively (and of course quantitatively) different from the curves from the non-dissipative linear theory. For example, the curves in figure 7 from the non-dissipative VNLS theory corresponding to experiments 1M, 2M and 6M show a bound on the growth of sidebands due to nonlinear interactions within the first 150 cm of evolution, but the measured data do not follow these curves. The measured data for experiments 1M, 2M and 6M are better predicted by the dissipative δ -VNLS theory. The physical experiments, experiments 1M–4M and 6M, are better predicted by the dissipative nonlinear theory. Experiments 5M and 7M have fairly small damping, so that the predictions of early evolution from the nonlinear dissipative and non-dissipative theories are nearby each other. This nearness is also true for predictions from the linear theory shown in figure 6. The linearized theories, shown in figure 6, predict faster growth of the primary sidebands than do the nonlinear theories, shown in figure 7. So, in experiments 5M and 7M, both dissipation and nonlinearity are important in the first 150 cm of evolution.

Column (c) of figure 7 shows comparisons of the nonlinear predictions and measurements of the carrier-wave amplitude over the first 150 cm of evolution. No such comparison is shown for the linearized models because the carrier-wave amplitude is necessarily constant in these models. Allowing for nonlinear interactions shows that again, the dissipative nonlinear theory does a better job of predicting

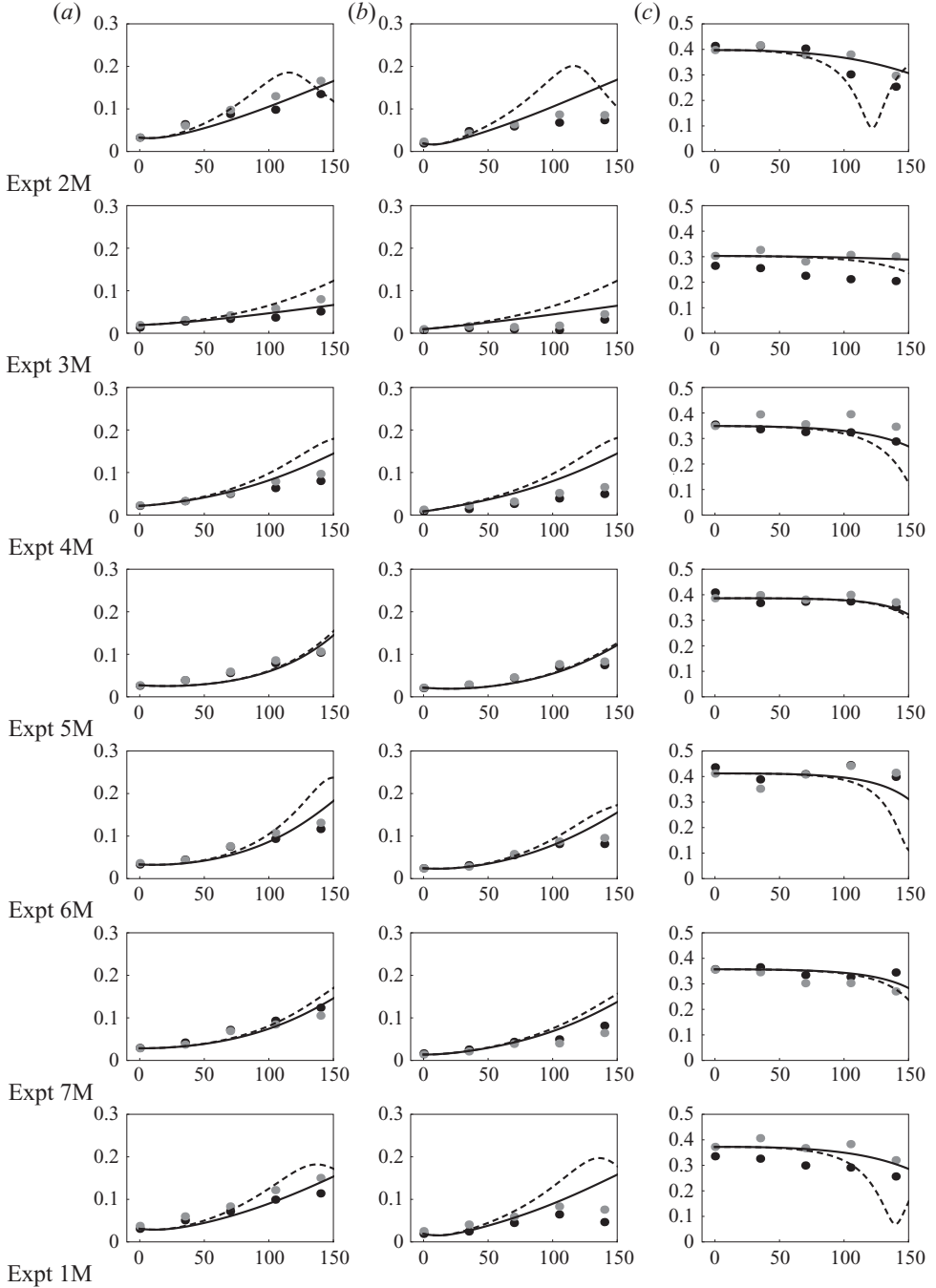


FIGURE 7. Measurements (dots), multiplied by $e^{\sigma^2 \delta x}$ and also shown in figure 6, and predictions (curves) from computations of (2.36) of the amplitudes of the lower (a) and upper (b) seeded sidebands from the two gauges in the antinodal region to the left (black) and right (grey) of the centreline of the wave tank. Column (c) shows measurements and predictions of the carrier-wave amplitudes. The solid curves are from the dissipative theory. The dashed curves are from the non-dissipative theory. The dissipation rate used for each row is listed in table 2 for the corresponding experiment. Graphs of (a) $|a_{-1}|$ (cm), (b) $|a_1|$ (cm) and (c) $|a_0|$ (cm) as functions of x (cm).

experimental results than does the nonlinear non-dissipative theory. In experiments 1M, 2M, 4M and 6M, predictions from the dissipative nonlinear theory (solid curves) and non-dissipative nonlinear theory (dashed curves) are qualitatively different. Note that in each of these experiments, the dissipative theory predicts the measured data much more accurately than does the non-dissipative theory. In general, the dissipative nonlinear theory, like the dissipative linear theory, predicts the qualitative and quantitative features of initial evolution better than the non-dissipative theory.

Finally, we note that short-crested waves, like those shown in figure 1, need not obey Melville's (1982) criterion for breaking of (long-crested) plane waves. In his study of breaking of plane waves on deep water, Melville (1982) found wave breaking for values of initial steepness ak from about 0.16 to 0.29, where $k(=2\pi/\lambda)$ is the wavenumber and $a=0.5(\bar{a}_{max} - \bar{a}_{min})$ is the wave amplitude. Later experimental studies (e.g. Tulin & Waseda 1999) found even lower threshold values for breaking. Note from table 2 that our 'moderate-amplitude' experiments had values of a from about 0.31 to 0.50 cm; so with $\lambda=10$ cm, our waves had ak varying from about 0.20 to 0.31, which goes above Melville's criterion for (plane) wave breaking. Even so, we observed no wave breaking in these experiments. How to generalize Melville's criterion for wave breaking to short-crested waves seems to be an open question at this time.

4.2. Large-amplitude experiments

What happens if wave amplitudes are larger? Here we discuss an experiment, 8L, in which we used the same wavemaker forcing as in experiments 1M, 2M, 4M and 7M, except that we doubled the ratio of perturbation amplitude to carrier-wave amplitude at the wavemaker (see table 1). Figure 8 shows the time series from the three gauges at x_i $\{i=1, \dots, 5\}$, while figure 9 shows the corresponding Fourier transforms. The perturbation is more visible at the first measurement site in this experiment and evolved asymmetrically as seen by the enhanced growth of the lower sideband in figure 9. There was also non-monotonic growth in the nodal line. Figure 10 shows the measurements of M , which use $\sigma^2\delta=0.128 \text{ m}^{-1}$ in (3.2).

A possible scenario for the perturbation evolution is that if its amplitude is large enough, nonlinearity becomes important and bounds further growth, dominating the effects of dissipation. However, the experiments show something entirely different: frequency downshifting occurs when nonlinearity becomes important enough, contrary to the prediction of either VNLS-type model, with or without dissipation. The Fourier transforms at x_1 , shown in figures 9(a)–9(c), show that the peak of the spectrum is at the carrier-wave frequency of 4 Hz. But by x_5 (figures 9m–9o) the peak shifted to the lower sideband at frequency 3.43 Hz. This result is consistent with the measurements of P_x , shown in figure 10(b), which become monotonically more negative. Gordon (1986) first used P (a scalar for plane waves) to measure the amount of frequency downshifting for experiments in nonlinear optics. We note that even if the dissipation rate were unknown, one could see that the P -integral did not behave as predicted by any NLS-type model. No positive dissipation rate allows the components of P to change sign, or to start at $P=0$ and have a component become increasingly negative. So figure 10(b) shows behaviour that is impossible for any NLS-type model.

The VNLS model (with $\delta=0$) predicts that the integral P is constant; the δ -VNLS model, (2.7), predicts that P is constant, and the original dissipative model, (2.2), before the overall damping is factored out by (2.3) or (2.6), predicts that the corresponding integral decays exponentially with the same rate as the dissipative analogue of $M(x)$: $(2\sigma^2\delta)$. The experimental result in figure 10(b) contradicts all of

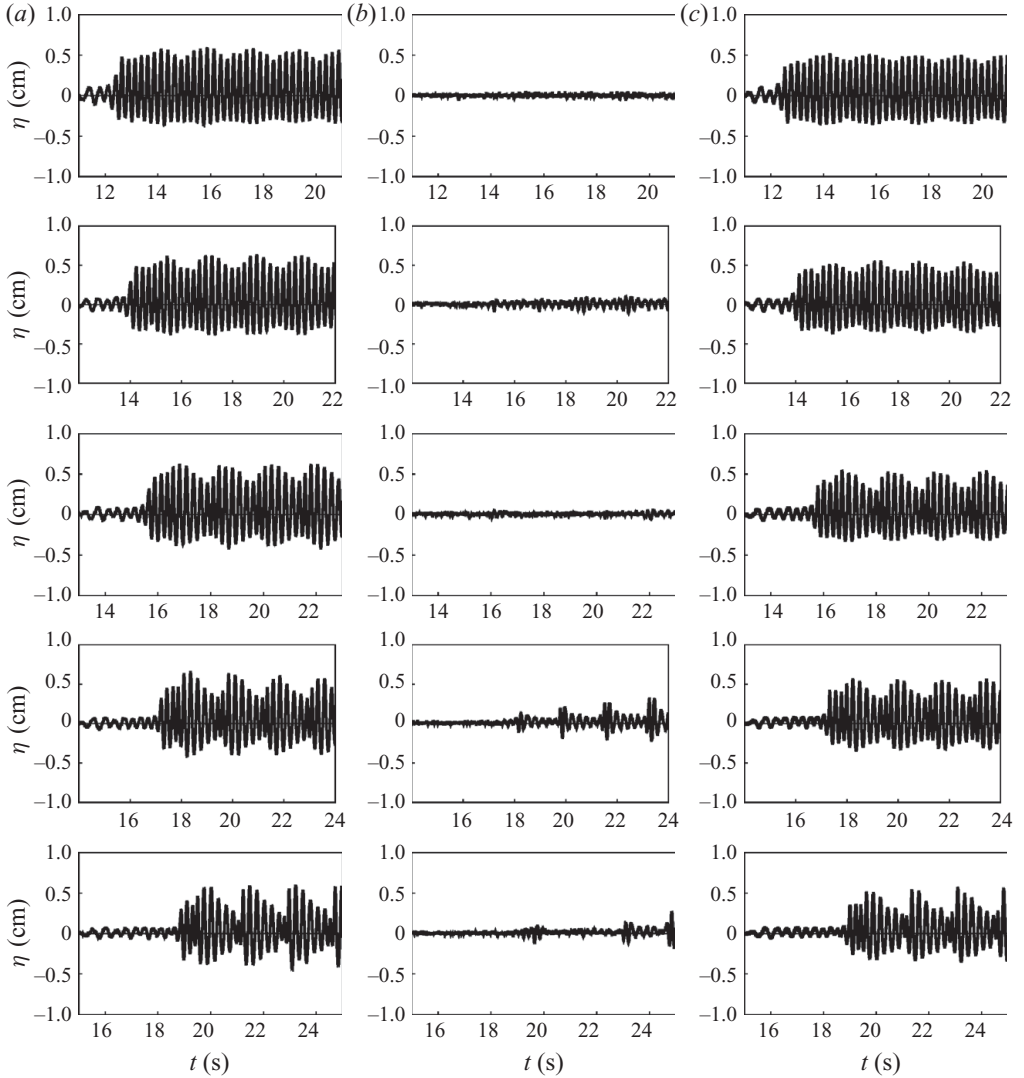


FIGURE 8. Experiment 8L. Water surface displacement as a function of time for gauges in the (nodal) centreline of the tank (*b*) and in the centre of the antinodal regions on its left side (*a*) and right side (*c*) at the five measuring stations, which were 35 cm apart.

these predictions. It shows that when the perturbation amplitude is large enough, both V-NLS models, with or without dissipation, fail to correctly predict the evolution of the integral \mathcal{P} . The shifting of the spectral peak to $\omega - \omega_p$ is an example of downshifting, a phenomenon that was first observed in water waves (Lake *et al.* 1977) and later in optics (Mitschke & Mollenauer 1986). A review of downshifting in water waves is given by Dias & Kharif (1999). We also observe this downshifting in experiments in which we increase only the carrier-wave amplitudes.

Both the frequency shift and the associated variation in \mathcal{P} were observed in Segur *et al.* (2005) and were proposed as measures of when an NLS model is/is not a valid

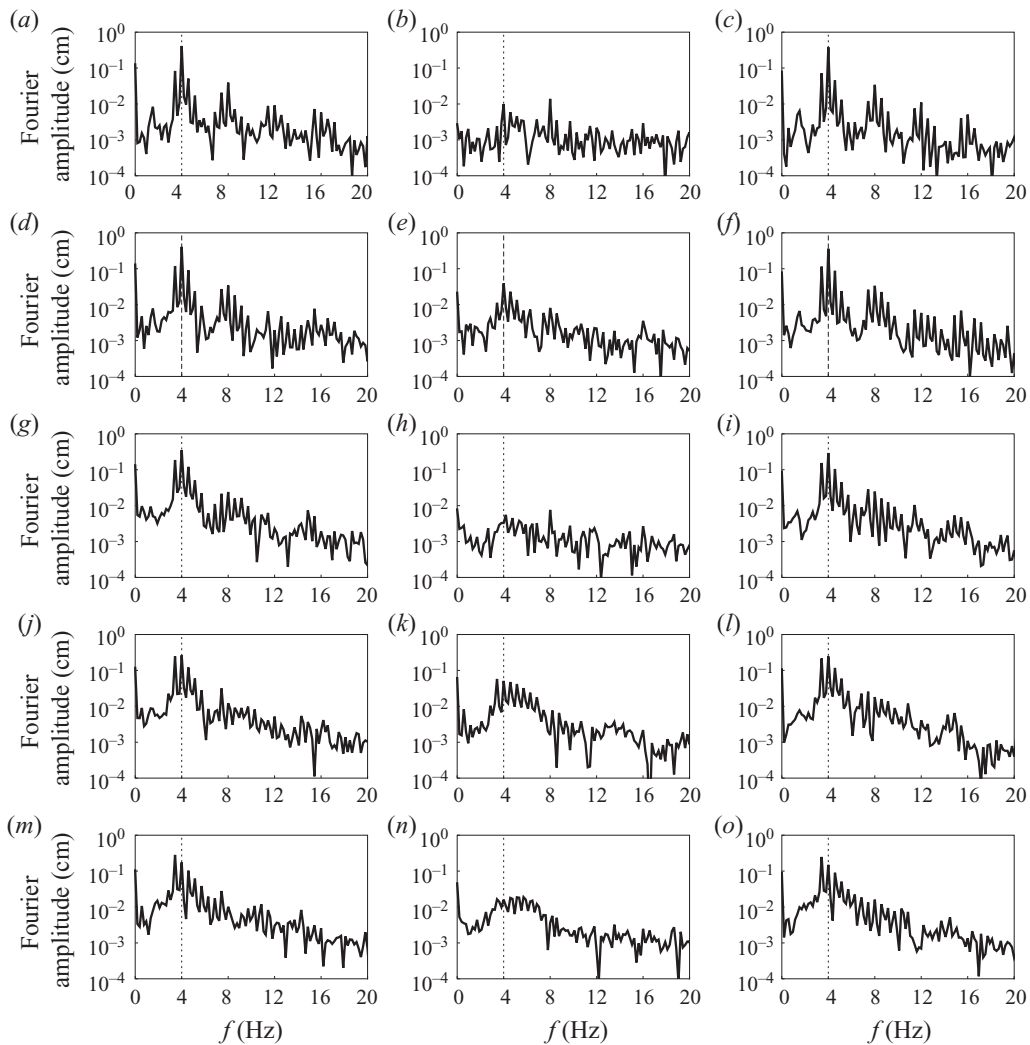


FIGURE 9. Experiment 8L. Fourier transforms of the data shown in figure 8 with respect to cyclic frequency f . The dashed vertical line is at the carrier-wave frequency $f = \omega/2\pi = 4$ Hz.

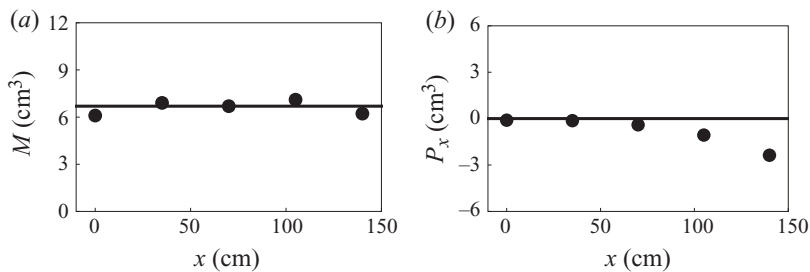


FIGURE 10. Measurements (dots) of (a) M and (b) P_x . The horizontal lines depict exponential decay at a rate of $\sigma^2\delta = 0.128 \text{ m}^{-1}$ in this system.

model for the evolution of plane waves. We reiterate that here: if M and P do not show the same exponential decay rate, then coupled NLS equations are not a valid model for deep-water waves.

5. Conclusions

In this paper, we consider two models for the evolution of bi-periodic patterns of deep-water waves: the VNLS equations with dissipation added in *a posteriori* and the δ -VNLS equations, which include dissipation *ab initio*. The non-dissipative VNLS model predicts that a uniform-amplitude pattern is unstable to modulational perturbations. The dissipative δ -VNLS model predicts that a uniform-amplitude pattern is stable to modulational perturbations. We show eight sets of experiments: seven in which the carrier-wave-perturbation combination had moderate amplitudes and one in which the carrier-wave-perturbation combination had a large amplitude.

For the moderate-amplitude experiments, the dissipative δ -VNLS model describes the experimental results more accurately than does the non-dissipative VNLS model, even after that model is corrected for dissipation. This difference in accuracy shows up in two different ways.

(i) Experimental tests of the linearized stability analyses show (in figures 5 and 6) that the dissipative model predicts the measured evolution of sidebands more accurately than does the non-dissipative model with a dissipative correction. In seven different experiments, whenever the two models give different predictions, the δ -VNLS model is more accurate. The δ -VNLS model predicts that two-dimensional wave patterns on deep water are linearly stable, and the superior accuracy of this model leads to the title of this paper.

(ii) Experimental tests of the two nonlinear models, without linearizing, are shown in figure 7. Again, whenever the two nonlinear models give different predictions, the δ -VNLS model is more accurate.

For the large-amplitude experiments, neither model proves adequate because a quantity (P_x) that is predicted to be conserved by both models is not conserved in the experiments. Our experiments show that when this quantity is not conserved, downshifting, which is not predicted by either model, occurs. For this reason we conclude that VNLS-type models are inadequate for large-amplitude wave pattern evolution. Which model should replace VNLS-type models (or NLS-type models for single carrier waves) for evolution of large-amplitude waves is an open question.

We thank the referees, whose comments significantly improved the paper, R. Geist for assisting with the experimental apparatus and the National Science Foundation for support through grants NSF-DMS-FRG-0139847, NSF-DMS-FRG 0139742, NSF-DMS 0708352 and NSF-DMS 0709415.

Appendix A. VNLS coefficients in the presence of surface tension

In (2.2), the coefficients ζ_{AB} and ζ_{BA} provide a measure of the coupling between the A and B wavetrains. These coefficients are given below and correct errors in the version given by Hammack *et al.* (2005). In the limit of zero surface tension, the coefficients given below agree with those given by Dhar & Das (1991) and later by

Onorato *et al.* (2006) (except for a misprint there):

$$\begin{aligned}
 \left(\frac{\kappa_B \sigma_B}{\omega_B}\right)^2 \zeta_{AB} = & -\frac{1}{2\Gamma_A \Gamma_B} \left[2\omega_B \Gamma_A (k_A k_B + l_A l_B) (\kappa_A \sigma_A + 2\kappa_B \sigma_B) + 2\omega_A \kappa_B^2 \omega_B^2 \right. \\
 & \left. - \omega_A \kappa_B \sigma_B \tau [2(k_A k_B + l_A l_B)^2 + \kappa_A^2 \kappa_B^2] \right] + \frac{\kappa_A \kappa_B^2 \omega_A (\sigma_A^2 - 1) (\sigma_B^2 - 1)}{2g\sigma_A} \\
 & + \frac{G - J}{2\kappa_A \sigma_A} [\omega_A (k_A k_B + l_A l_B) - \kappa_A \sigma_A \kappa_B \sigma_B \omega_B] + \frac{iF}{2} \left[k_B (k_A + k_B) \right. \\
 & \left. + l_B (l_A + l_B) + \frac{\omega_B \Gamma_A}{\omega_A \Gamma_B} (k_A (k_A + k_B) + l_A (l_A + l_B)) - \kappa_+ \sigma_+ \omega_A \frac{\omega_B}{\Gamma_B} \right] \\
 & - \frac{iH}{2} \left[k_B (k_A - k_B) + l_B (l_A - l_B) + \frac{\omega_B \Gamma_A}{\omega_A \Gamma_B} (k_A (k_A - k_B) \right. \\
 & \left. + l_A (l_A - l_B)) - \kappa_- \sigma_- \omega_A \frac{\omega_B}{\Gamma_B} \right],
 \end{aligned}$$

$$\begin{aligned}
 \left(\frac{\kappa_A \sigma_A}{\omega_A}\right)^2 \zeta_{BA} = & -\frac{1}{2\Gamma_A \Gamma_B} \left[2\omega_A \Gamma_B (k_A k_B + l_A l_B) (\kappa_B \sigma_B + 2\kappa_A \sigma_A) + 2\omega_B \kappa_A^2 \omega_A^2 \right. \\
 & \left. - \omega_B \kappa_A \sigma_A \tau [2(k_A k_B + l_A l_B)^2 + \kappa_A^2 \kappa_B^2] \right] + \frac{\kappa_A^2 \kappa_B \omega_B (\sigma_A^2 - 1) (\sigma_B^2 - 1)}{2g\sigma_B} \\
 & + \frac{G - J}{2\kappa_B \sigma_B} [\omega_B (k_A k_B + l_A l_B) - \kappa_A \sigma_A \kappa_B \sigma_B \omega_A] + \frac{iF}{2} \left[k_A (k_A + k_B) \right. \\
 & \left. + l_A (l_A + l_B) + \frac{\omega_A \Gamma_B}{\omega_B \Gamma_A} (k_B (k_A + k_B) + l_B (l_A + l_B)) - \kappa_+ \sigma_+ \omega_B \frac{\omega_A}{\Gamma_A} \right] \\
 & - \frac{iH}{2} \left[k_A (k_A - k_B) + l_A (l_A - l_B) + \frac{\omega_A \Gamma_B}{\omega_B \Gamma_A} (k_B (k_A - k_B) \right. \\
 & \left. + l_B (l_A - l_B)) + \kappa_- \sigma_- \omega_B \frac{\omega_A}{\Gamma_A} \right],
 \end{aligned}$$

where

$$\begin{aligned}
 \kappa_{A/B} &= \sqrt{k_{A/B}^2 + l_{A/B}^2}, & \kappa_{\pm} &= \sqrt{(k_A \pm k_B)^2 + (l_A \pm l_B)^2}, \\
 \sigma_{A/B} &= \tanh \kappa_{A/B} h, & \sigma_{\pm} &= \tanh \kappa_{\pm} h, \\
 \Gamma_{A/B} &= g + \tau \kappa_{A/B}^2, & \Gamma_{\pm} &= g + \tau \kappa_{\pm}^2, \\
 \omega_{A/B}^2 &= \kappa_{A/B} \Gamma_{A/B} \sigma_{A/B}, & \omega_{\pm}^2 &= \kappa_{\pm} \Gamma_{\pm} \sigma_{\pm},
 \end{aligned}$$

$$F = -i \frac{\kappa_A \sigma_A \kappa_B \sigma_B (\omega_A + \omega_B) - \frac{\omega_A \omega_B}{\Gamma_A \Gamma_B} (\omega_A + \omega_B)^3 + (\Gamma_+ - \tau (k_A k_B + l_A l_B)) \left(\frac{\omega_A}{\Gamma_A} (\kappa_+^2 - \kappa_A^2) + \frac{\omega_B}{\Gamma_B} (\kappa_+^2 - \kappa_B^2) \right)}{\omega_+^2 - (\omega_A + \omega_B)^2},$$

$$H = -i \frac{\kappa_A \sigma_A \kappa_B \sigma_B (\omega_A - \omega_B) + \frac{\omega_A \omega_B}{\Gamma_A \Gamma_B} (\omega_A - \omega_B)^3 + (\Gamma_- + \tau (k_A k_B + l_A l_B)) \left(\frac{\omega_A}{\Gamma_A} (\kappa_-^2 - \kappa_A^2) - \frac{\omega_B}{\Gamma_B} (\kappa_-^2 - \kappa_B^2) \right)}{\omega_-^2 - (\omega_A - \omega_B)^2},$$

Experiment	σS_1 (cm)	σS_2 (cm)
1M	0.00478 - 0.00300i	0.00125 - 0.00274i
2M	-0.00217 - 0.00564i	-0.00245 - 0.00126i
3M	-0.00264 + 0.00211i	0.001744 + 0.000256i
4M	-0.00319 + 0.00116i	0.00196 + 0.00122i
5M	0.000709 - 0.00102i	-0.0000708 - 0.00601i
6M	0.00132 + 0.00000i	0.00389 - 0.00602i
7M	0.00160 + 0.000889i	0.002752 - 0.004501i

TABLE 6. Initial values of σS_1 and σS_2 for all experiments.

Experiment	σD_1 (cm)	σD_2 (cm)
1M	-0.000120 + 0.000238i	-0.000312 - 0.0000677i
2M	-0.000108 + 0.000122i	0.000106 - 0.000332i
3M	0.000134 + 0.0000448i	0.000246 - 0.0000767i
4M	-0.000261 - 0.000212i	0.000361 - 0.000325i
5M	-0.0000754 - 0.000524i	0.0000708 + 0.000280i
6M	-0.0000739 + 0.000113i	0.000112 + 0.000207i
7M	-0.000463 + 0.000289i	-0.000580 - 0.000327i

TABLE 7. Initial values of σD_1 and σD_2 for all experiments.

$$G = \frac{1}{\omega_+^2 - (\omega_A + \omega_B)^2} \left[(\omega_A + \omega_B) \left\{ \frac{\omega_A}{\Gamma_A} (k_B(k_A + k_B) + l_B(l_A + l_B)) + \frac{\omega_B}{\Gamma_B} (k_A(k_A + k_B) + l_A(l_A + l_B)) \right\} + \kappa_+ \sigma_+ \left(k_A k_B + l_A l_B + \kappa_A \sigma_A \kappa_B \sigma_B - \frac{\omega_A \omega_B}{\Gamma_A \Gamma_B} (\omega_A + \omega_B)^2 \right) \right],$$

$$J = \frac{-1}{\omega_-^2 - (\omega_A - \omega_B)^2} \left[(\omega_A - \omega_B) \left\{ \frac{\omega_A}{\Gamma_A} (k_B(k_A - k_B) + l_B(l_A - l_B)) + \frac{\omega_B}{\Gamma_B} (k_A(k_A - k_B) + l_A(l_A - l_B)) \right\} + \kappa_- \sigma_- \left(k_A k_B + l_A l_B - \kappa_A \sigma_A \kappa_B \sigma_B - \frac{\omega_A \omega_B}{\Gamma_A \Gamma_B} (\omega_A - \omega_B)^2 \right) \right].$$

Appendix B. Initial conditions

The initial conditions used for computations of (2.21) are listed in tables 6 and 7. The initial conditions for numerical computations of (2.7) rewritten as (2.36) are obtained from these values as described in §2.2.

REFERENCES

- ANDERSON, D. & LISAK, M. 1984 Modulational instability of coherent optical-fibre transmission signals. *Opt. Lett.* **9**, 468–470.
- BALUDIN, S. I., SHRIRA, V. I., KHARIF, C. & IOUALALEN, M. 1995 On two approaches to the problem of instability of short-crested water waves. *J. Fluid Mech.* **303**, 297–326.
- BENJAMIN, B. & FEIR, J. 1967 The disintegration of wavetrains in deep water. Part 1. *J. Fluid Mech.* **27**, 417–430.
- BENJAMIN, T. B. 1967 Instability of periodic wavetrains in nonlinear dispersive systems. *Proc. R. Soc. Lond. A* **299**, 59–75.
- BENNEY, D. J. & NEWELL, A. C. 1967 The propagation of nonlinear wave envelopes. *J. Math. Phys. (Stud. Appl. Math.)* **46**, 133–139.

- BRIDGES, T. J. & LAINE-PEARSON, F. E. 2005 The long-wave instability of short-crested waves, via embedding in the oblique two-wave interaction. *J. Fluid Mech.* **543**, 147–182.
- CHAPPELEAR, J. E. 1959 A class of three-dimensional shallow water waves. *J. Geophys. Res.* **64**, 1883–1890.
- CRAIG, W., HENDERSON, D. M., OSCAMOU, M. & SEGUR, H. 2007 Stable three-dimensional waves of nearly permanent form on deep water. *Math. Comput. Simul.* **74**, 135–144.
- CRAIG, W. & NICHOLLS, D. 2000 Travelling two and three dimensional capillary gravity water waves. *SIAM: J. Math. Anal.* **32**, 323–359.
- CRAIG, W. & NICHOLLS, D. 2002 Travelling gravity waves in two and three dimensions. *Eur. J. Mech. B/Fluids* **21**, 615–641.
- DAVIES, J. T. & VOSE, R. W. 1965 On the damping of capillary waves by surface films. *Proc. R. Soc. Lond. A* **260**, 218–233.
- DHAR, A. K. & DAS, K. P. 1991 Fourth-order nonlinear evolution equations for two Stokes wave trains in deep water. *Phys. Fluids A* **3**, 3021–3026.
- DIAS, F., DYACHENKO, A. I. & ZAKHAROV, V. E. 2008 Theory of weakly damped free-surface flows: a new formulation based on potential flow solutions. *Phys. Lett. A* **372**, 1297–1302.
- DIAS, F. & KHARIF, C. 1999 Nonlinear gravity and capillary-gravity waves. *Annu. Rev. Fluid Mech.* **31**, 301–346.
- DYSTHE, K. B. 1979 Note on a modification to the nonlinear Schrödinger equation for application to deep water waves. *Proc. R. Soc. Lond. A* **369**, 105–114.
- FUCHS, R. A. 1952 On the theory of short crested oscillatory waves. In *Gravity Waves*. 521, pp. 187–200. United States National Bureau of Standards.
- FUHRMAN, D. R. & MADSEN, P. A. 2006 Short-crested waves in deep water: a numerical investigation of recent laboratory experiments. *J. Fluid Mech.* **559**, 391–411.
- FUHRMAN, D. R., MADSEN, P. A. & BINGHAM, H. B. 2006 Numerical simulation of lowest-order short-crested wave instabilities. *J. Fluid Mech.* **563**, 415–441.
- GORDON, J. P. 1986 Theory of the soliton self-frequency shift. *Opt. Lett.* **11**, 662–664.
- HAMMACK, J. L., HENDERSON, D. M. & SEGUR, H. 2005 Progressive waves with persistent two-dimensional surface patterns in deep water. *J. Fluid Mech.* **532**, 1–52.
- HAMMACK, J. L., SCHEFFNER, N. & SEGUR, H. 1989 Two-dimensional periodic waves in shallow water. *J. Fluid Mech.* **209**, 567–589.
- HASEGAWA, A. 1972 Theory and computer experiment on self-trapping instability of plasma cyclotron waves. *Phys. Fluids* **15**, 870–881.
- HASEGAWA, A. & KODAMA, Y. 1995 *Solitons in Optical Communications*. Clarendon Press.
- HENDERSON, D. M. 1998 Effects of surfactants on Faraday-wave dynamics. *J. Fluid Mech.* **365**, 89–107.
- HENDERSON, D., PATTERSON, M. S. & SEGUR, H. 2006 On the laboratory generation of two-dimensional, progressive, surface waves of nearly permanent form on deep water. *J. Fluid Mech.* **559**, 413–427.
- HUHNERFUSS, H., LANGE, P. & WALTER, W. 1985 Relaxation effects in monolayers and their contribution to water wave damping. Part II. The Marangoni phenomenon and gravity wave attenuation. *J. Colloid Interface Sci.* **108**, 442–450.
- IOOSS, G. & PLOTNIKOV, P. 2009 Small divisor problem in the theory of three-dimensional water gravity waves. *Mem. AMS* **200** (940), 128 pp.
- IOUALALEN, M. & KHARIF, C. 1994 On the subharmonic instabilities of steady three-dimensional deep water waves. *J. Fluid Mech.* **262**, 265–291.
- KARLSSON, M. 1995 Modulational instability in lossy optical fibers. *J. Opt. Soc. Am. B* **12**, 2071–2077.
- KIMMOUN, O., BRANGER, H. & KHARIF, C. 1999 On short-crested waves: experimental and analytical investigations. *Eur. J. Mech. B/Fluids* **18**, 889–930.
- LAKE, B. M., YUEN, H. C., RUNGALDIER, H. & FERGUSON, W. E. 1977 Nonlinear deep-water waves: theory and experiment. Part 2. Evolution of a continuous wave train. *J. Fluid Mech.* **83**, 49–74.
- LEBLANC, S. 2009 Stability of bichromatic gravity waves on deep water. *Eur. J. Mech. B/Fluids* **28**, 605–612.
- LUCASSEN, J. 1982 Effect of surface-active material on the damping of gravity waves: a reappraisal. *J. Colloid Interface Sci.* **85**, 52–58.

- LUTHER, G. G. & MCKINSTRIE, C. J. 1990 Transverse modulational instability of collinear waves. *J. Opt. Soc. Am. B* **7**, 1125–1141.
- MCKINSTRIE, C. J. & BINGHAM, R. 1989 The modulational instability of coupled waves. *Phys. Fluids B* **1**, 230–237.
- MEL, C. C. & HANCOCK, M. J. 2003 Weakly nonlinear surface waves over a random seabed. *J. Fluid Mech.* **475**, 247–268.
- MELVILLE, W. K. 1982 The instability and breaking of deep-water waves. *J. Fluid Mech.* **115**, 165–185.
- MILES, J. W. 1967 Surface-wave damping in closed basins. *Proc. R. Soc. Lond. A* **297**, 459–475.
- MITSCHKE, F. M. & MOLLENAUER, L. F. 1986 Discovery of the soliton self-frequency shift. *Opt. Lett.* **11**, 659–661.
- NYMITSKII, V. V. & STEPANOV, V. V. 1960 *Qualitative Theory of Differential Equations*. Princeton University Press.
- ONORATO, M., OSBORNE, A. R. & SERIO, M. 2006 Modulational instability in crossing sea states: a possible mechanism for the formation of freak waves. *Phys. Rev. Lett.* **96**, 014503.
- OSTROVSKY, L. A. 1967 Propagation of wave packets and space-time self-focussing in a nonlinear medium. *Sov. J. Exp. Theor. Phys.* **24**, 797–800.
- PIERCE, R. D. & KNOBLOCH, E. 1994 On the modulational instability of travelling and standing water waves. *Phys. Fluids* **6**, 1177–1190.
- RAYLEIGH, L. 1890 On the tension of water surfaces, clean and contaminated, investigated by the method of ripples. *Phil. Mag.* **XXX**, 386–400.
- ROSKES, G. J. 1976 Nonlinear multiphase deep-water wavetrains. *Phys. Fluids*. **19**, 1253–1254.
- SEGUR, H., HENDERSON, D., CARTER, J., HAMMACK, J., LI, C.-M., PHEIFF, D. & SOCHA, K. 2005 Stabilizing the Benjamin–Feir instability. *J. Fluid Mech.* **539**, 229–271.
- SHUKLA, P. K., KOURAKIS, I., ELIASSON, B., MARKLUND, M. & STENFLO, L. 2006 Instability and evolution of nonlinearly interacting water waves. *Phys. Rev. Lett.* **97**, 094501.
- STOKES, G. G. 1847 On the theory of oscillatory waves. *Trans. Camb. Phil. Soc.* **8**, 441.
- STOKES, G. G. 1966 *Mathematical and Physical Papers*, vol. 1. Johnson Reprint Corp.
- TAI, K., TOMITA, A. & HASEGAWA, A. 1986 Observation of modulational instability in optical fibres. *Phys. Rev. Lett.* **56**, 135–138.
- TULIN, M. P. & WASEDA, T. 1999 Laboratory observations of wave group evolution, including breaking effects. *J. Fluid Mech.* **378**, 197–232.
- ZAKHAROV, V. E. 1967 Instability of self-focusing of light. *Sov. J. Exp. Theor. Phys.* **24**, 455–459.
- ZAKHAROV, V. E. 1968 Stability of periodic waves of finite amplitude on the surface of a deep fluid. *J. Appl. Mech. Tech. Phys.* **2**, 190–194.